

## Acoustic resonators above 100 GHz

Jack Kramer<sup>1</sup>, Bryan T. Bosworth<sup>2\*</sup>, Lezli Matto<sup>3\*</sup>, Nicholas R. Jungwirth<sup>2\*</sup>, Omar Barrera<sup>1</sup>,  
Florian Bergmann<sup>2,4</sup>, Sinwoo Cho<sup>1</sup>, Vakhtang Chulukhadze<sup>1</sup>, Mark Goorsky<sup>3</sup>,  
Nathan D. Orloff<sup>2\*</sup>, and Ruochen Lu<sup>1</sup>

<sup>1</sup>The University of Texas at Austin, Austin, 78712, TX, USA.

<sup>2</sup>National Institute of Standards and Technology, Boulder, 80305, CO, USA.

<sup>3</sup>University of California, Los Angeles, Los Angeles, 90095, CA, USA

<sup>4</sup>Department of Physics, University of Colorado, Libby Dr, Boulder, Colorado 80302, USA

\*These authors contributed equally to the work.

### Abstract

Piezoelectric resonators are a common building block for signal processing<sup>1-3</sup> because of their miniature size, low insertion loss, and high quality factor. As consumer electronics push to millimeter waves<sup>4</sup> frequencies, designers must increase the operating frequency of the resonator. The current state-of-the-art approach to increase the operating frequency is to decrease the thickness<sup>5,6</sup> of the piezoelectric film to shorten the acoustic wavelength or to use higher order modes<sup>7,8</sup>. Unfortunately, maintaining high crystal quality typically requires thicker piezoelectric layers<sup>9</sup>. Thinner layers suffer from higher defect densities and increased surface damping, which degrade the electromechanical coupling and quality factor. While acoustic high order modes can also increase operating frequency, the electromechanical coupling rapidly

decreases with increasing mode number. Here, we overcome these limitations by utilizing a piezoelectric stack of three layers of lithium niobate with alternating crystallographic orientations to preferentially support higher order modes and thereby enhance the electromechanical coupling without degrading the quality factor. Our approach improves the figure of merit of millimeter-wave acoustic resonators by roughly an order of magnitude greater compared to state-of-the-art piezoelectric resonators above 60 GHz. This concept of alternating crystallographic orientations facilitates a new path to develop millimeter wave resonators with high figures of merit, low insertion loss, and miniature footprints, enabling new applications in millimeter wave signal processing and computing.

## Main

### Introduction

Piezoelectric materials couple electrical and mechanical fields<sup>10</sup>. By designing acoustic cavities from piezoelectric materials, engineers can create acoustic resonators that are orders of magnitude smaller than equivalent electromagnetic cavities and that take advantage of the low loss provided by acoustic waves<sup>2,3,11,12</sup>. These acoustic resonators are important building blocks for telecommunication filters<sup>1,13</sup>, oscillators<sup>14,15</sup>, acousto-optic modulators<sup>16-18</sup>, and even quantum circuits<sup>19,20</sup>. Often the thickness defines the frequency of operation of the thin film acoustic cavity more than other geometry parameters<sup>11</sup> (Fig 1). Ranging from micrometers to hundreds of nanometers (Fig 1a), typical film thicknesses produce resonators that operate in the megahertz (MHz) to gigahertz (GHz) frequency ranges<sup>11,21</sup>. Thinner films can achieve higher operating frequencies, but fabrication induced defect densities and surface damping<sup>9,22</sup> increase

with decreasing film thickness (Fig 1b). Defects degrade acoustic performance and result in poor electrical to mechanical transduction and reduced cavity finesse, quantified by the electromechanical coupling ( $k^2$ ) and quality factor ( $Q$ ), respectively<sup>11,12</sup>. One alternative to reducing film thicknesses is to use higher order acoustic modes (Fig 1a). Unfortunately, high order modes in an acoustic resonator reduce the electromechanical coupling since the sign of the local strain fails to match the crystal lattice orientation<sup>8</sup> (Fig. 1c), leading to charge cancellation. Consequently, acoustic resonators above 10 GHz tend to suffer from reduced figures of merit ( $k^2Q$ ) (Fig 1b). Achieving a relatively high figure of merit in acoustic resonators in the tens and hundreds of GHz remains an open challenge. Solving this challenge could enable compact millimeter-wave communication front ends, high-speed integrated photonic modulation, and high-fidelity quantum phononic states.

Transferred and bonded thin-film lithium niobate (LN) may offer a few solutions to help overcome some of the limitations in conventional acoustic resonators. First, the crystal quality of the transferred LN remains comparable to the bulk even at film thickness, which have relatively high defect densities when compared to deposited materials<sup>23</sup>. The transferred LN can also leverage low loss dielectric substrates with arbitrary crystal structure and orientation to reduce parasitic electromagnetic losses. Moreover, a sacrificial layer below the transferred LN can further confine acoustic energy within the cavity due to a high acoustic impedance mismatch between LN and air<sup>24,25</sup>. The last remaining challenge is the reduced electromechanical coupling of a high order mode resonator using a single-layer LN (Fig 1c). To overcome this, various researchers have begun examining using multiple layers of piezoelectric materials with alternating crystallographic orientation to address this challenge<sup>26–32</sup>. Alternating the

crystallographic orientation of the piezoelectric material could match the local electric field profile to the strain among layers, resulting in a constructive contribution to the electromechanical coupling. If realized through a thin film transfer process, independent selection of the independent layer crystallographic orientation could be made without needing to consider the substrate crystalline structure. Through this approach, transferred LN in multiple layers with tailored thicknesses and crystallographic orientation has the potential to push the technology envelope embodied by the tradeoff between operating frequency and the acoustic figure of merit—electromechanical coupling ( $k^2$ ) times quality factor (Q)—above 100 GHz (Fig. 1d).

Here, we test an approach to design acoustic resonators above 100 GHz by transferring multiple LN layers into a three-layer stack with alternating crystallographic orientations. After transferring, we validate the crystal quality of each layer in the multilayer stack. We discuss the codesign and co-fabrication of acoustic resonators with microwave calibration kits, enabling the acoustic response to be de-embedded from electromagnetic effects. We perform S-parameter microwave characterization of the acoustic resonators with on-wafer techniques to 220 GHz. From the measured data, we observe electrically excited acoustic modes from 16 to 120 GHz, enabled by the multilayer LN. Beyond 60 GHz, the extracted figures of merit exceed the state-of-the-art. With further optimization and integration, the multilayer LN stack platform advances toward the viable deployment of miniature acoustic devices above 100 GHz. To our knowledge, this work represents the highest frequency demonstration of electrically excited acoustic resonators.

## Multilayer LN stack

To enable acoustic resonances above 100 GHz, we chose three layers of alternating LN to target the 3<sup>rd</sup>, 9<sup>th</sup>, 15<sup>th</sup> and 21<sup>st</sup> order thickness shear modes (Fig. 2a, b). In a three-layer LN stack, the superlattice preferentially supports the 3<sup>rd</sup> order mode with the latter modes being the higher order modes that also provide the highest electromechanical coupling. To optimize for the 3<sup>rd</sup> shear mode, we selected 128Y cut LN layers for the maximum value of the shear  $e_{15}$  component of the electromechanical coupling matrix. The ideal configuration of the multilayer LN consists of alternating upwards and downwards facing 128Y cut LN layers (Fig. 2a) that have been aligned such that their crystallographic X-axis are rotated 180° opposite one another. Proper alignment of the crystallographic orientations is important for mitigating the excitation of additional acoustic modes and for maximizing the electromechanical coupling of the targeted shear modes. To achieve the ideal electromechanical coupling for the shape of the 3<sup>rd</sup> order shear mode, alternating layers were nearly equal in film thicknesses relative to each other (Fig. 2b). This thickness requirement made it challenging to realize practical multilayer transferred LN<sup>9</sup>. It is possible that additional layers could improve the figure of merit of higher order modes; however, we expect some degradation in the figure of merit as the thickness of the transferred LN approaches the effective thickness of the interfacial layer (Fig. 2c).

Our idea assumes that the process of micromachining and transferring each LN layer does not impact crystal quality and the interfacial material properties are negligible. The bright field scanning transmission electron microscopy (STEM) showed three distinct LN layers and confirmed their respective thicknesses (Fig. 2b). While we observed slight differences in layer thicknesses, each layer remained within the regime where we expected enhanced

electromechanical coupling. At the interfaces of the LN layers (Fig 2c), we observed the alternating crystallographic orientation of the LN. Both electron diffraction patterns and Fourier transform (SFig. 1) of the lattice images from the alternating layers (FFT) produced reciprocal space diffraction patterns for each layer and showed the expected upwards and downwards facing 128Y cut LN orientations (Fig. 2d). To further ensure the correct crystallographic orientations and crystalline properties, we performed various high-resolution X-ray diffraction (HR-XRD) scans about different axes (Fig. 2e). An HR-XRD  $\phi$  scan validated the in-plane rotation of the LN layers, which displays a  $183^\circ$  rotation of the intermediate layer X-axis orientation relative to the top and bottom layers.

We observed an in-plane misalignment of less than  $1^\circ$  for the top and bottom layers relative to each other. Using an HR-XRD  $\omega:2\theta$  scan, we extracted film thicknesses through the spatial separation of the thin film interference fringes for each of the layers (Fig. 2f). The observed fringe spacing corresponds to thicknesses of 98 nm, 98 nm, and 87 nm for LN layers 1, 2, and 3 respectively, using the nomenclature in Figure 2. The layer thickness differences are very small considering the bonding, lapping and chemical mechanical polishing (CMP) steps used to create each layer in succession across a 4-inch wafer. The measurement location of the BF-STEM and HR-XRD differed slightly from each other, resulting in slight variation in thickness between the two methods. HR-XRD rocking curve measurements verified that the transferred LN crystal retained its initial quality after the thinning process. The various layers had full width at half maximum (FWHM) peaks ranging from 45 to 260 arcseconds, confirming the high overall crystalline quality of these layers (SFig. 2). These small FWHM values show that the LN quality is

preserved through the formation of the multilayer LN stack, potentially enabling high performance acoustic resonators.

### High frequency acoustic resonators

Today, on-wafer metrology above 100 GHz is not routine because the required measurement equipment is uncommon. On-wafer calibration kits should be tailored to the application<sup>33</sup> (SFig. 3). Above 100 GHz, one must also consider the resonator (SFig. 4b,c) along with the de-embedding test structures (SFig. 4d-g) during design to accurately characterize the response of the acoustic cavity (Fig. 3). Isolating the acoustic cavity both electrically and mechanically from the environment helped maximize the quality factors and minimize parasitic modes. Our acoustic resonator consisted of an acoustic cavity and an aluminum microwave transmission line (Fig. 3a) electrically designed to minimize radiation and surface waves<sup>34</sup>. An air gap (Fig 3a) mechanically decoupled the acoustic cavity from the substrate. The interdigitated aluminum electrodes electrically excited the acoustic waves in the cavity. We selected aluminum for its comparatively low resistivity, low density, and its compatibility with the sacrificial layer etch process (Supplemental, SFig. 5). 50  $\mu\text{m}$  pitch ground-signal-ground probes electrically contacted each resonator, enabling measurement with an ultrabroadband 220 GHz vector network analyzer (VNA) (Supplemental, SFig. 6).

The ultrabroadband measurement used a two-tier calibration approach from 10 MHz to 220 GHz. The first tier was an off-chip calibration on sapphire with a custom on-wafer calibration kit that had nominally identical cross-sectional dimensions as the transmission lines on our resonators. The line lengths of the first-tier calibration minimized the uncertainty in the

calibration over the bandwidth<sup>33</sup>. This first-tier calibration translated the measurement reference plane to the probe tips and set the reference impedance to  $50 \Omega$ . Next, we performed a second-tier calibration with the on-wafer calibration kit, which was also designed to minimize the uncertainty in the calibration. This second-tier calibration translated the reference plane to the resonator (Fig. 3b). We cascaded the first and second tier calibrations to correct the measurements of the acoustic resonators. The measured broadband response showed resonant peaks associated with acoustic modes from 10 GHz to 120 GHz (Fig 3c).

The strongest coupling acoustic resonance near 16 GHz corresponds to the enhanced 3<sup>rd</sup> order shear mode, with the next target modes being the peaks at roughly 50, 80, and 115 GHz. Adjacent to the target modes, there are acoustic resonances corresponding to the  $n \pm 1$  order shear modes. These adjacent modes theoretically receive significantly lower electromechanical coupling than the target modes, but the practical value fluctuates with the relative layer thicknesses within the multilayer LN stack (SFig. 7, SFig. 8). The general character of the curve (Fig. 3c) is consistent with an electromagnetic resonance at roughly 100 GHz. A series inductance in the tapered transmission line and the static capacitance of the transducer electrodes were the dominant causes of this electromagnetic effect (SFig. 9). We confirmed that the frequency of this electromagnetic resonance depends directly on the acoustic resonator geometry (SFig. 10, STable 2) and the corresponding impact on these two values. As an example, we noted that increased electrode spacing leads to higher frequency electromagnetic resonances due to the reduced static capacitance (SFig. 11). Using the measured device data, we construct a multibranch modified Butterworth-Van Dyke circuit model of the acoustic resonator (SFig. 9) that extracts (STable 1) the quality factor ( $Q$ ) and electromechanical coupling ( $k^2$ ) of each represented



resonance. The circuit fitting extracted the performance metrics instead of employing 3dB Q or other methods due to interplay of mechanical and electrical effects that lead to distorted raw extraction metrics.

The acoustic resonators on transferred multilayer LN demonstrated comparable quality factors (Fig. 4a) with enhanced electromechanical coupling (Fig. 4b) relative to the state-of-the-art (grey dashed line, Fig. 4a,b). The extracted quality factors for the given modes remained comparable to the state-of-the-art (Fig. 4b). The measured enhanced coupling (Fig. 4b) upholds the hypothesis that the multilayer LN stack preferentially supports acoustic modes where the sign of the local strain matches the crystal lattice orientation in each layer. The resultant figure of merit (blue dashed line, Fig. 4c) represents a significant improvement when compared to the state-of-the-art (grey dashed line, Fig. 4c).

## Conclusion

These results underscore the achievable improvement possible in millimeter wave acoustics through the preferential enhancement of high order modes with multilayer lithium niobate with alternating crystallographic orientation. This approach achieves higher electromechanical coupling to enable higher figures of merit and the highest frequency demonstration of electrically excited acoustic resonators, to the best of our knowledge. The figure of merit improvement achieved creates an opportunity for multilayer lithium niobate resonators and filters above 100 GHz. For example, our 49 GHz resonance with high figure of merit of 7 could enable a filter with an insertion loss of 2.4 dB and a fractional bandwidth 4.6%, reducing the receiver amplifier power by over half (SFig. 12). Especially for spaceborne

applications, we estimate this filter would weigh only 750  $\mu\text{g}$ , compared to approximately 40g for space-qualified cavity filters. Additionally, efficient high frequency acoustic transduction could allow on-chip photonic mixers and modulators, or higher temperature hybrid quantum circuits. For example, from Bose-Einstein statistics, we estimate that our 114 GHz resonance has less than 1% thermal occupation probability at 1.2K, while a 1 GHz resonance would require a temperature below 10.5mK to achieve this thermal occupation. The multilayer lithium niobate topology could be further expanded to include more layers or layers of different thicknesses, orientations, or even different materials. More generally, the multilayer transfer approach could be advantageous for enabling thin film systems with substantially different properties from a single layer counterpart. The multilayer transfer approach opens the doors for expanding the functionality of thin film technology.

## Methods

For this study, we diced 2.1 by 1.9 cm samples of the multilayer LN stack from the 4-inch wafer provided by NGK Insulators Inc. We worked with NGK Insulators Inc. to attempt to minimize interfacial damage and layer nonuniformity with this prototype wafer. NGK Insulators Inc. performed the multistep bonding and polishing of bulk 128°Y LN wafers that were then characterized in house. We performed HR-XRD scans using a Bruker / Jordan Valley D1 diffractometer with both incident and scattered beam optics<sup>35</sup> and STEM images on smaller diced pieces taken from the edge of the wafer, roughly 1.5 by 2 cm in size. We prepared the TEM sample with a focused ion beam tool, and the TEM imaging with an FEI 300 keV Titan<sup>36</sup>. For the FIB sample preparation, we evaporated gold and platinum layers followed by an additional layer of ion beam deposited platinum to protect the surface during FIB milling. We produced cross-

section images to extract layer thicknesses and to assess the crystallography perfection and orientation across the interfaces. We performed HR-XRD scans towards the center of this sample and near the diced pieces at a location furthest from the wafer edge (1.5-2 cm from the wafer periphery). We selected the rocking curve,  $\phi$ , and  $\omega:2\theta$  scans to characterize the crystal quality, sample orientation alignment, and layer thicknesses, respectively. The rocking curve measurement showed FWHM values of 260, 190, and 45 arcseconds for layers 1 through 3 respectively. We compared these values to bulk LN values of roughly 60 arcseconds, indicating that crystal quality is largely preserved through the LN layer transfer process. The high-quality transfer is important towards reducing phonon scattering sites associated with crystal lattice imperfections.

For this study we considered an array of acoustic resonator designs, utilizing previous iterations of resonators targeting roughly 50 GHz operation as a benchmark for predicted 100 GHz operation. We provide the terminology used for the various cavity parameters in supplementary information (SFig. 9). We swept a range of acoustic lateral wavelengths ranging from 6 to 20 micrometers. For each wavelength, we varied electrode widths from 600 to 1400 nm. For each lateral acoustic wavelength and electrode width, we varied aperture lengths from 45, 55, and 65 micrometers. We considered two electrode thicknesses of 250 and 350 nm to examine the effects of electrical and mechanical loading. Due to the observed layer variation in the material analysis, we placed 6 copies of the cavity parameter set across the sample piece. We included the on-chip calibration kits on the perimeter of the sample. We fabricated the devices with standard microfabrication techniques (SFig. 4,5).

Due to the extensive time required to perform measurements beyond 100 GHz, we initially characterized the devices with a 67 GHz using an Agilent E8361C PNA Network Analyzer. We calibrated the system to the probe tips using a commercial GGB CS-5 calibration kit, and then two-port S-parameters were measured. We examined the 67 GHz measurements to determine the 9th order mode at roughly 50 GHz, which acts as a benchmark for the predicted performance of the 15th and 21st order modes. Using these measurements, we selected a subset of 16 devices for high frequency measurement. We performed these measurements by first using an in-house fabricated calibration kit on sapphire to calibrate the system to the probe tips. Then, we extracted  $y$  parameters for the transmission line structure with the measurement of the on-chip calibration kit. We performed the device measurements similarly, with a 10 MHz to 220 GHz span set with 5 MHz point spacing and 100 intermediate frequency bandwidth. Once measured, we translate the reference plane from the probe tips to the tapered region using the second-tier calibration.

## Data availability

The datasets generated in this study are available upon reasonable request to the corresponding author.

## References

1. Ruby, R. A Snapshot in Time: The Future in Filters for Cell Phones. *IEEE Microw. Mag.* **16**, 46–59 (2015).
2. Hashimoto, K. *Surface Acoustic Wave Devices in Telecommunications*. (Springer, Berlin, Heidelberg, 2000). doi:10.1007/978-3-662-04223-6.

3. Hagelauer, A. *et al.* Microwave Acoustic Wave Devices: Recent Advances on Architectures, Modeling, Materials, and Packaging. *IEEE Trans. Microw. Theory Tech.* **66**, 4548–4562 (2018).
4. Hagelauer, A. *et al.* From Microwave Acoustic Filters to Millimeter-Wave Operation and New Applications. *IEEE J. Microw.* **3**, 484–508 (2023).
5. Bousquet, M. *et al.* Single-mode high frequency LiNbO<sub>3</sub> Film Bulk Acoustic Resonator. in *2019 IEEE International Ultrasonics Symposium (IUS)* 84–87 (2019). doi:10.1109/ULTSYM.2019.8925617.
6. Park, M., Wang, J., Wang, D., Mi, Z. & Ansari, A. A 19 GHz All-Epitaxial Al<sub>0.8</sub>Sc<sub>0.2</sub>N Cascaded FBAR for RF Filtering Applications. *IEEE Electron Device Lett.* **45**, 1341–1344 (2024).
7. Schaffer, Z., Simeoni, P. & Piazza, G. 33 GHz Overmoded Bulk Acoustic Resonator. *IEEE Microw. Wirel. Compon. Lett.* **32**, 656–659 (2022).
8. Yang, Y., Lu, R., Gao, L. & Gong, S. 10–60-GHz Electromechanical Resonators Using Thin-Film Lithium Niobate. *IEEE Trans. Microw. Theory Tech.* **68**, 5211–5220 (2020).
9. Lu, R., Yang, Y. & Gong, S. Acoustic Loss in Thin-Film Lithium Niobate: An Experimental Study. *J. Microelectromechanical Syst.* **30**, 632–641 (2021).
10. Auld, B. A. *Acoustic Fields and Waves in Solids*. (Krieger Publishing Company, 1990).
11. Hashimoto, K. *RF Bulk Acoustic Wave Filters for Communications*. (Artech House, 2009).
12. Gong, S., Lu, R., Yang, Y., Gao, L. & Hassanien, A. E. Microwave Acoustic Devices: Recent Advances and Outlook. *IEEE J. Microw.* **1**, 601–609 (2021).
13. Giribaldi, G., Colombo, L., Simeoni, P. & Rinaldi, M. Compact and wideband nanoacoustic pass-band filters for future 5G and 6G cellular radios. *Nat. Commun.* **15**, 304 (2024).

14. Piazza, G., Felmetger, V., Muralt, P., Iii, R. H. O. & Ruby, R. Piezoelectric aluminum nitride thin films for microelectromechanical systems. *MRS Bull.* **37**, 1051–1061 (2012).
15. Hara, M. *et al.* Study of 3-GHz-band Thin-film Bulk Acoustic Resonator Oscillators for Microfabricated Atomic Clocks. in *2021 IEEE International Ultrasonics Symposium (IUS)* 1–4 (2021). doi:10.1109/IUS52206.2021.9593390.
16. Yang, Z. *et al.* Efficient acousto-optic modulation using a microring resonator on a thin-film lithium niobate–chalcogenide hybrid platform. *Opt. Lett.* **47**, 3808–3811 (2022).
17. Shao, L. *et al.* Microwave-to-optical conversion using lithium niobate thin-film acoustic resonators. *Optica* **6**, 1498–1505 (2019).
18. Tian, H. *et al.* Hybrid integrated photonics using bulk acoustic resonators. *Nat. Commun.* **11**, 1–8 (2020).
19. Satzinger, K. J. *et al.* Quantum control of surface acoustic-wave phonons. *Nature* **563**, 661–665 (2018).
20. Wollack, E. A. *et al.* Quantum state preparation and tomography of entangled mechanical resonators. *Nature* **604**, 463–467 (2022).
21. Zou, Y. *et al.* Aluminum scandium nitride thin-film bulk acoustic resonators for 5G wideband applications. *Microsyst. Nanoeng.* **8**, 1–7 (2022).
22. Tabrizian, R., Rais-Zadeh, M. & Ayazi, F. Effect of phonon interactions on limiting the f.Q product of micromechanical resonators. in *TRANSDUCERS 2009 - 2009 International Solid-State Sensors, Actuators and Microsystems Conference* 2131–2134 (2009). doi:10.1109/SENSOR.2009.5285627.

23. *Piezoelectric MEMS Resonators*. (Springer International Publishing, Cham, 2017).  
doi:10.1007/978-3-319-28688-4.
24. Plessky, V. *et al.* 5 GHz laterally-excited bulk-wave resonators (XBARs) based on thin platelets of lithium niobate. *Electron. Lett.* **55**, 98–100 (2019).
25. Kadota, M. & Ogami, T. 5.4 GHz Lamb Wave Resonator on LiNbO<sub>3</sub> Thin Crystal Plate and Its Application. *Jpn. J. Appl. Phys.* **50**, 07HD11 (2011).
26. Koohi, M. Z. & Mortazawi, A. Negative Piezoelectric-Based Electric-Field-Actuated Mode-Switchable Multilayer Ferroelectric FBARs for Selective Control of Harmonic Resonances Without Degrading  $K_{eff}^2$ . *IEEE Trans. Ultrason. Ferroelectr. Freq. Control* **67**, 1922–1930 (2020).
27. Kramer, J. *et al.* Thin-Film Lithium Niobate Acoustic Resonator with High Q of 237 and  $k_2$  of 5.1% at 50.74 GHz. in *2023 Joint Conference of the European Frequency and Time Forum and IEEE International Frequency Control Symposium (EFTF/IFCS)* 1–4 (2023).  
doi:10.1109/EFTF/IFCS57587.2023.10272149.
28. Kramer, J. *et al.* Trilayer Periodically Poled Piezoelectric Film Lithium Niobate Resonator. in *2023 IEEE International Ultrasonics Symposium (IUS)* 1–4 (2023).  
doi:10.1109/IUS51837.2023.10306831.
29. Vetry, R. *et al.* A Manufacturable AlScN Periodically Polarized Piezoelectric Film Bulk Acoustic Wave Resonator (AlScN P3F BAW) Operating in Overtone Mode at X and Ku Band. in *2023 IEEE/MTT-S International Microwave Symposium - IMS 2023* 891–894 (2023).  
doi:10.1109/IMS37964.2023.10188141.

30. Mo, D., Dabas, S., Rassay, S. & Tabrizian, R. Complementary-Switchable Dual-Mode SHF Scandium Aluminum Nitride BAW Resonator. *IEEE Trans. Electron Devices* **69**, 4624–4631 (2022).
31. Izhar *et al.* A High Quality Factor, 19-GHz Periodically Poled AlScN BAW Resonator Fabricated in a Commercial XBAW Process. *IEEE Trans. Electron Devices* **71**, 5630–5637 (2024).
32. Peng, W., Nam, S., Wang, D., Mi, Z. & Mortazawi, A. A 56 GHz Trilayer AlN/ScAlN/AlN Periodically Poled FBAR. in *2024 IEEE/MTT-S International Microwave Symposium - IMS 2024* 150–153 (2024). doi:10.1109/IMS40175.2024.10600386.
33. Marks, R. B. A multiline method of network analyzer calibration. *IEEE Trans. Microw. Theory Tech.* **39**, 1205–1215 (1991).
34. Weis, R. S. & Gaylord, T. K. Lithium niobate: Summary of physical properties and crystal structure. *Appl. Phys. A* **37**, 191–203 (1985).
35. Waseda, Y., Matsubara, E. & Shinoda, K. *X-Ray Diffraction Crystallography: Introduction, Examples and Solved Problems*. (Springer, Berlin, Heidelberg, 2011). doi:10.1007/978-3-642-16635-8.
36. Chen, C. J. *Introduction to Scanning Tunneling Microscopy Third Edition*. (Oxford University Press, Oxford, New York, 2021).
37. Xie, J. *et al.* Sub-terahertz electromechanics. *Nat. Electron.* **6**, 301–306 (2023).
38. Park, M. *et al.* A 10 GHz Single-Crystalline Scandium-Doped Aluminum Nitride Lamb-Wave Resonator. in *2019 20th International Conference on Solid-State Sensors, Actuators and Microsystems & Eurosensors XXXIII (TRANSDUCERS & EUROSENSORS XXXIII)* 450–453 (2019). doi:10.1109/TRANSDUCERS.2019.8808374.



39. Link, S., Lu, R., Yang, Y., Hassanien, A. E. & Gong, S. An A1 Mode Resonator at 12 GHz using 160nm Lithium Niobate Suspended Thin Film. in *2021 IEEE International Ultrasonics Symposium (IUS)* 1–4 (2021). doi:10.1109/IUS52206.2021.9593341.
40. Lu, R., Yang, Y., Link, S. & Gong, S. A1 Resonators in 128° Y-cut Lithium Niobate with Electromechanical Coupling of 46.4%. *J. Microelectromechanical Syst.* **29**, 313–319 (2020).
41. Colombo, L., Kochhar, A., Vidal-Álvarez, G. & Piazza, G. Impact of Frequency Mismatch on the Quality Factor of Large Arrays of X-Cut Lithium Niobate MEMS Resonators. *J. Microelectromechanical Syst.* **29**, 1455–1463 (2020).
42. Mo, D., Dabas, S., Rassay, S. & Tabrizian, R. Complementary-Switchable Dual-Mode SHF Scandium Aluminum Nitride BAW Resonator. *IEEE Trans. Electron Devices* **69**, 4624–4631 (2022).
43. Faizan, M. & Villanueva, L. G. Frequency-scalable fabrication process flow for lithium niobate based Lamb wave resonators. *J. Micromechanics Microengineering* **30**, 015008 (2019).
44. Gong, S. & Piazza, G. Figure-of-Merit Enhancement for Laterally Vibrating Lithium Niobate MEMS Resonators. *IEEE Trans. Electron Devices* **60**, 3888–3894 (2013).
45. Kadota, M., Kuratani, Y., Kimura, T., Esashi, M. & Tanaka, S. Ultra-wideband and high frequency resonators using shear horizontal type plate wave in LiNbO<sub>3</sub> thin plate. *Jpn. J. Appl. Phys.* **53**, 07KD03 (2014).
46. Kimura, T., Omura, M., Kishimoto, Y. & Hashimoto, K. Comparative Study of Acoustic Wave Devices Using Thin Piezoelectric Plates in the 3–5-GHz Range. *IEEE Trans. Microw. Theory Tech.* **67**, 915–921 (2019).

47. Kochhar, A., Mahmoud, A., Shen, Y., Turumella, N. & Piazza, G. X-Cut Lithium Niobate-Based Shear Horizontal Resonators for Radio Frequency Applications. *J. Microelectromechanical Syst.* **29**, 1464–1472 (2020).
48. Assylbekova, M. *et al.* Study of the Performance Enhancement of Sc-Doped AlN Super High Frequency Cross-Sectional Lamé Mode Resonators. *Micromachines* **14**, (2023).
49. Gong, S. & Piazza, G. Overmoded shear horizontal wave MEMS resonators using X-cut lithium niobate thin film. in *2014 IEEE International Ultrasonics Symposium* 568–571 (2014). doi:10.1109/ULTSYM.2014.0140.
50. Olsson, R. H. *et al.* A high electromechanical coupling coefficient SH0 Lamb wave lithium niobate micromechanical resonator and a method for fabrication. *Sens. Actuators Phys.* **209**, 183–190 (2014).
51. Song, Y.-H. & Gong, S. Spurious mode suppression in SH0 Lithium Niobate laterally vibrating MEMS resonators. in *2015 IEEE International Electron Devices Meeting (IEDM)* 18.5.1-18.5.4 (2015). doi:10.1109/IEDM.2015.7409728.
52. Kramer, J. *et al.* 57 GHz Acoustic Resonator with  $k^2$  of 7.3 % and Q of 56 in Thin-Film Lithium Niobate. in *2022 International Electron Devices Meeting (IEDM)* 16.4.1-16.4.4 (2022). doi:10.1109/IEDM45625.2022.10019391.
53. Schaffer, Z., Hassanien, A., Masud, M. A. & Piazza, G. A Solidly Mounted 55 GHz Overmoded Bulk Acoustic Resonator. in *2023 IEEE International Ultrasonics Symposium (IUS)* 1–4 (2023). doi:10.1109/IUS51837.2023.10307494.

## Acknowledgement

The project was funded by DARPA COmpact Front-end Filters at the EIEment-level (COFFEE) project. The authors would like to thank Dr. Ben Griffin, Dr. Todd Bauer, and Dr. Zachary Fishman for their helpful discussions. The authors would like to acknowledge the helpful discussions with Dr. Keji Lai, Dr. David Burghoff, Dr. Ari Feldman, and Dr. Jeffrey Jargon during the preparation of the manuscript.

## Author contributions

The resonators were designed by J.K., R.L., and N.D.O. The resonator fabrication process was developed and performed by J.K., O.B., S.C., and V.C. The material analysis, including STEM and XRD, were performed and analyzed by L.M. and M.G. The microwave measurements and characterization were performed by B.T.B., N.R.J., and F.B. The microwave data analysis was performed by J.K., N.D.O., M.G., and R.L. wrote the manuscript. R.L., N.D.O. and J.K. conceived and designed the study. All others discussed and commented on the manuscript.

## Competing interests

The authors declare no competing interest.

## Corresponding author

Correspondence to Jack Kramer (kramerj99@utexas.edu)

# Main Figures:

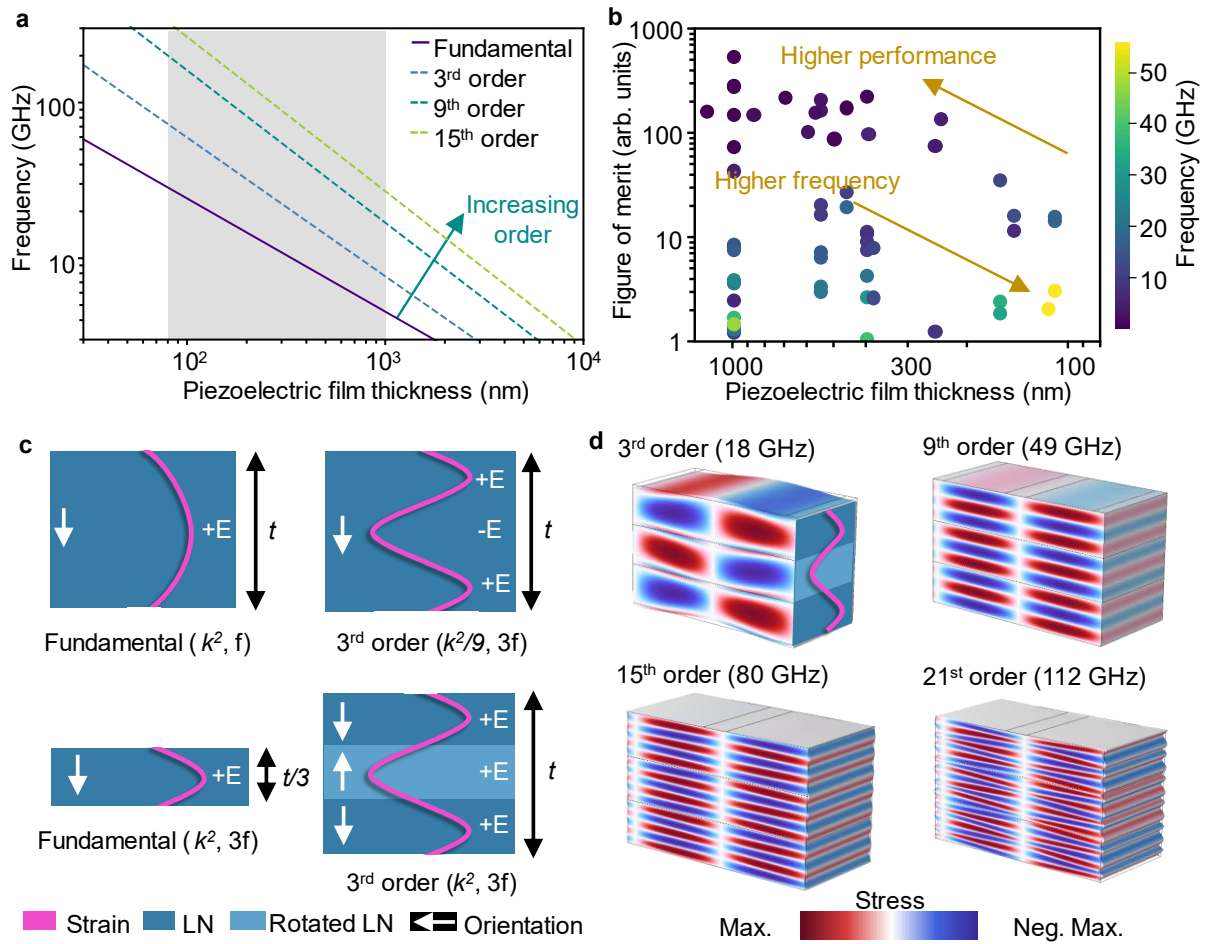


Figure 1 | **a** Plot of acoustic mode resonant frequency as a function of piezoelectric film thickness. The limit of achievable high quality thin film piezoelectrics is highlighted in gray. Advancing to higher mode order significantly increases the achievable operational resonant frequency. **b** Survey of reported acoustic resonator figure of merit<sup>5–8,24,27–29,31,32,37–53</sup>. Figure of merit is defined as the quality factor,  $Q$ , times the electromechanical coupling,  $k^2$ . Thicker piezoelectric films yield higher figures of merit, while thinner films are required for high resonant frequency operation. **c** Illustration of impact of piezoelectric thickness,  $t$ , and crystal orientation on resonant frequency,  $f$ , and electromechanical coupling,  $k^2$ . Increasing mode order from the fundamental to the 3rd order triples the resulting resonant frequency, but at the cost of electromechanical coupling. Electromechanical coupling is reduced due to cancellation in the electric field,  $E$ , in the piezoelectric associated with the modal strain. The same frequency can also be achieved by reducing the thickness of the film, at the cost of quality factor and performance shown in **b**. However, electromechanical coupling and piezoelectric thickness are both maintained if the orientation of the piezoelectric is alternated such that the associated electric field adds constructively. **d** Simulated modal profiles for the 4 target modes in a three-layer lithium niobate. The modal profiles correspond to the 3rd, 9th, 15th and 21st thickness shear modes.

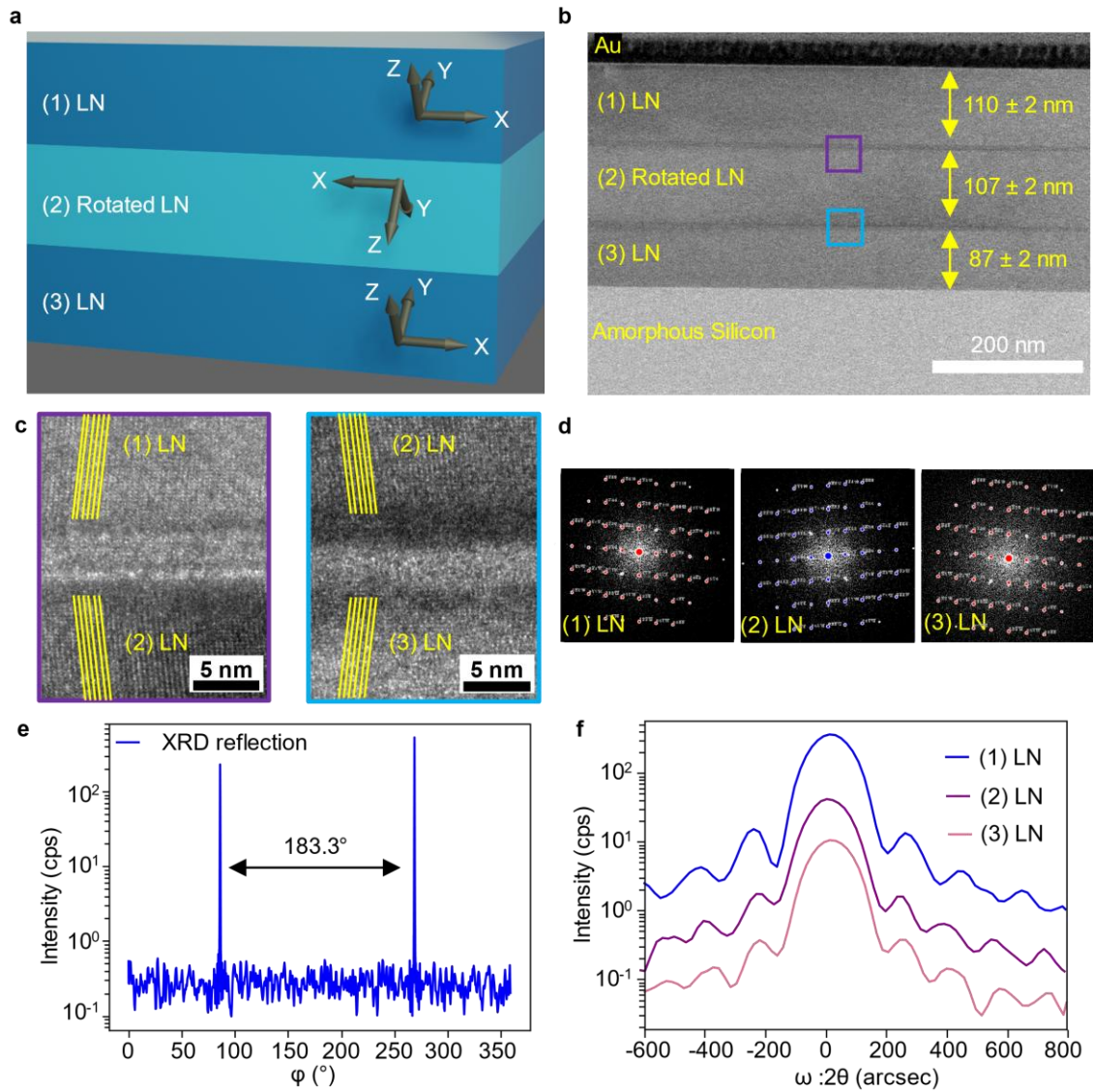


Figure 2 | **a** Illustration of the multilayer lithium niobate stack with alternating crystal orientations. The crystal orientation of each layer is indicated by the illustrated axis. **b** Bright field scanning transmission electron microscope image of the multilayer lithium niobate stack. The purple and blue outlined regions correspond to the high-resolution scanning transmission electron shown in panel **c**. **c** High resolution STEM images of layer interfaces, showing alternating crystallographic orientations. An amorphous interfacial layer from the bonding process is also observed. **d** Superimposed observed and simulated electron diffraction patterns of the individual lithium

niobate layers. The red and blue dots correspond to the simulated diffraction patterns, while the white dots are the observed diffraction patterns. **e**  $\phi$  x-ray diffraction scan measurement of the multilayer lithium niobate stack. Two peaks are observed, corresponding to the two desired crystal orientations, offset by 183.3 degrees. The two peaks confirm the in-plane orientation of the layers is close to the desired 180-degree offset. The reduced first peak is due to the existence of two closely spaced peaks, associated with layers (1) and (3) of the lithium niobate. More information is supplied in supplementary information. **f**  $\omega:2\theta$  x-ray diffraction scan of the multilayer stack. Each of the three layers displays strong fringes associated with preserved high crystal quality.

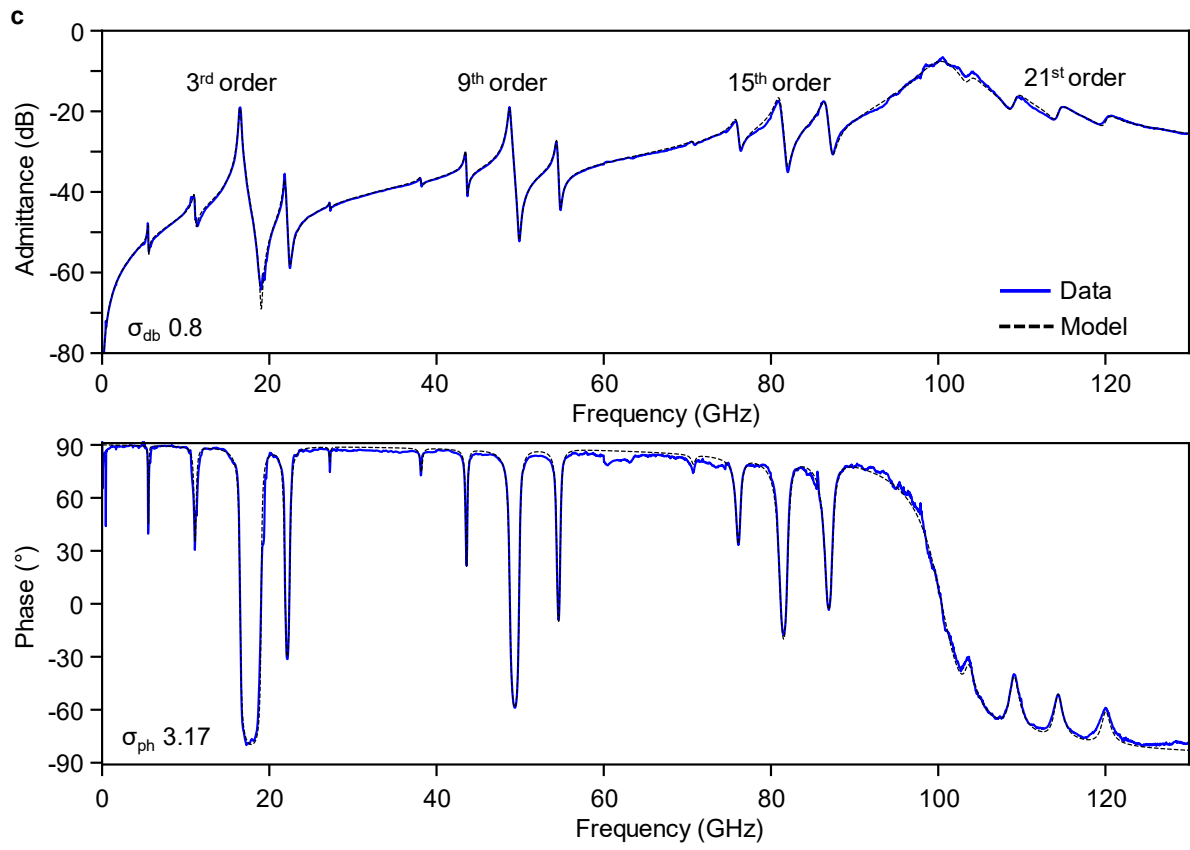
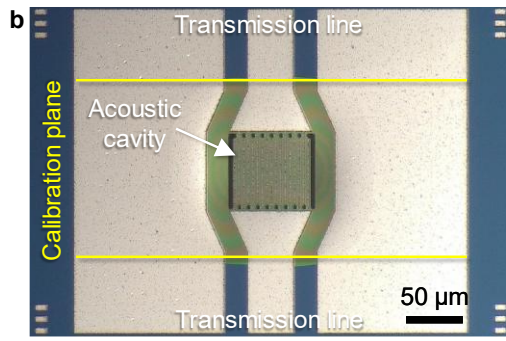
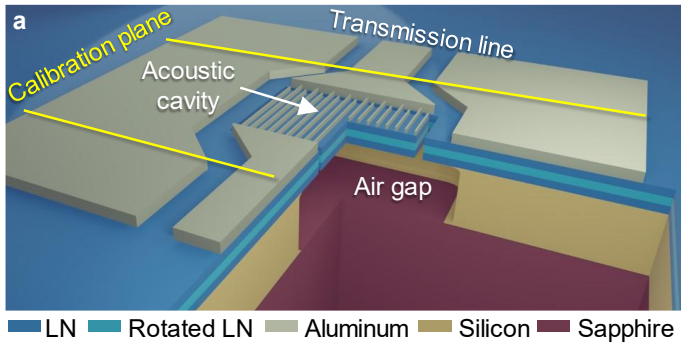




Figure 3 | **a** Illustration of the acoustic resonator topology. An acoustic cavity is formed, isolated from the rest of the multilayer stack and the substrate with air gaps. The cavity is actuated by aluminum electrodes that span across the surface. A microwave transmission line allows for on-chip measurements using a vector network analyzer. An on-chip calibration kit with matching dimensions allows for the translation of the calibration plane to the tapered transmission line region. Details are provided in the supplementary information. **b** Optical micrograph of the fabricated acoustic cavity. The region that has been isolated from the substrate is indicated by the change in color, from blue to yellow, of the film. **c** Broadband admittance measurement of the acoustic resonator. Resonant modes are observed up to 120 GHz. The targeted 3rd, 9th, 15th and 21st order modes show the strongest peaks, associated with the large electromechanical coupling. Adjacent modes are also observed neighboring the target modes. These are associated with thickness variance between individual lithium niobate layers, with additional information provided in the supplementary. The model uses a 17-branch modified Butterworth-van Dyke circuit and is used for device performance extraction. Details are provided in the supplementary.

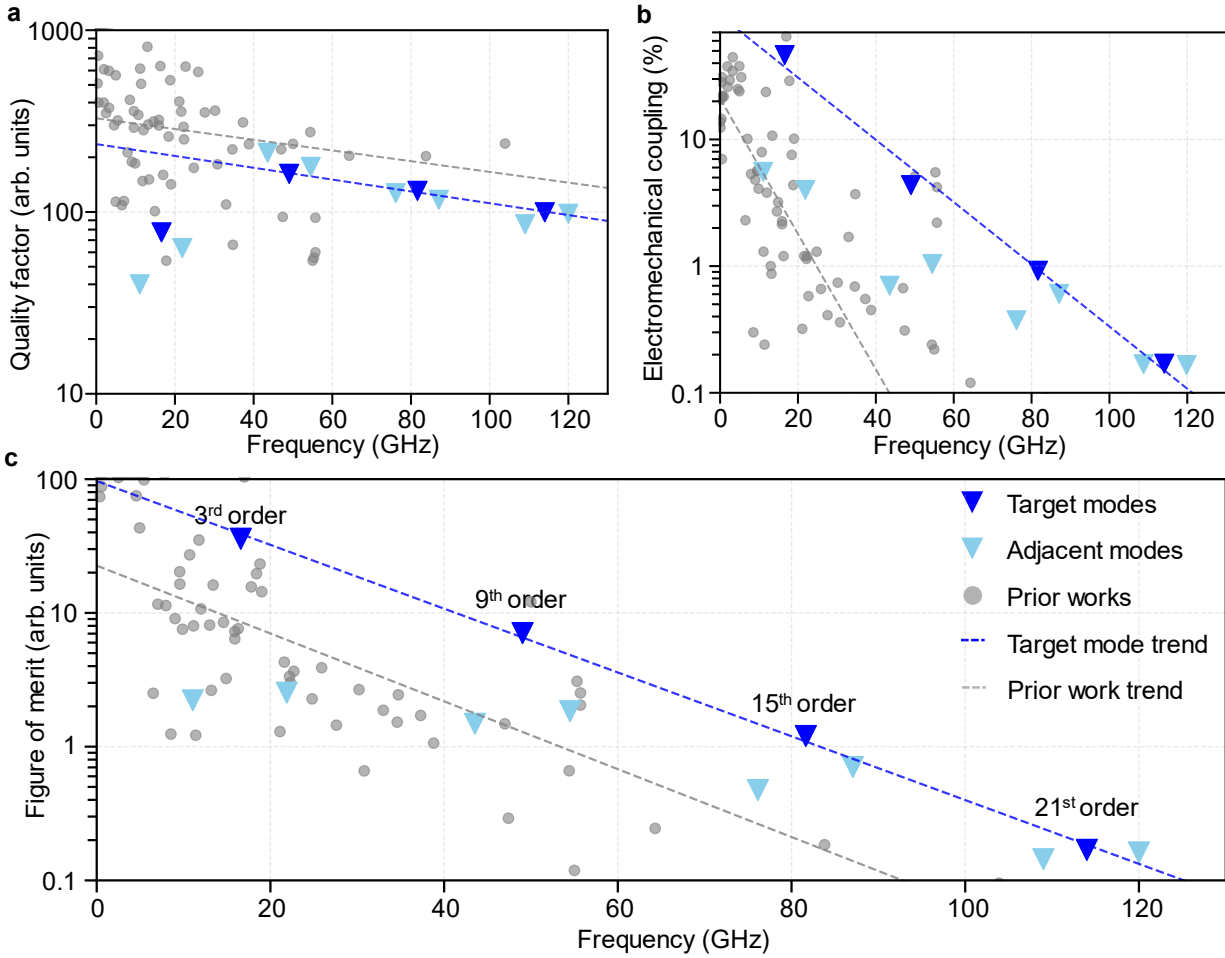


Figure 4 | **a, b, c** Plot of quality factor, electromechanical coupling, and figure of merit respectively, for the target modes and adjacent modes. An additional survey of prior works<sup>5–8,24,27–29,31,32,37–53</sup> is also included for reference. A robust linear fitting, which neglects statistical outliers, is applied to target modes and prior work to provide the data trend. Higher electromechanical couplings are achieved through the multilayer lithium niobate platform. Quality factors are comparable, on the order 200 and degrade to 100 for the modes beyond 100 GHz. The combination allows for a higher resultant figure of merit, particularly for the target modes towards and beyond 100 GHz.

## Supplementary Information

### 1.1 Fabrication

The realization of the multilayer LN stack is accomplished through a multistep transfer, lapping, and chemical mechanical polishing (CMP) process. First, one micron of amorphous silicon is deposited onto a bare 128Y cut lithium niobate wafer. This is then bonded to the sapphire wafer such that the bonding occurs at the amorphous silicon and sapphire interface. Then, the lithium niobate layer is thinned to the target thickness using CMP. The next layer is bonded directly to the first LN layer and similarly thinned to the target thickness with CMP. This is repeated for the third LN layer to achieve the final multilayer stack.

We employ standard fabrication procedures to create the devices used in the study (SFig. 5). First, we dice the 4-inch wafer into sample pieces of 2.1 by 1.9 cm. We pattern etch windows using photolithography, which defines the extents of the resonant cavity. Next, we use electron beam lithography to pattern the electrode and busline features. We use electron beam evaporation to deposit 250 nm of aluminum, which is then lifted off using acetone and sonication. Another round of electron beam lithography patterning, evaporation and lift-off adds 350 nm of aluminum to the busline features of the devices. This enables better probe contact during measurement, ensuring good transmission between the microwave probe tip and the device. As discussed in methods, we explore a large range of cavity parameters for this study. Due to the dependence on individual LN layer thickness for coupling performance, we include copies of the devices to 6 regions of the sample. Including devices at multiple locations helps account for the

local thickness variations across the sample. The GDS file layout for the mask, as well as example devices, are given in SFig. 4.

## 1.2 Calibration and Measurement

After fabrication, we perform an initial characterization up to 67 GHz using an Agilent E8361C PNA Network Analyzer with 1.85 mm coaxial cables running to 100  $\mu\text{m}$  pitch GGB Industries GSG microwave probes. We measure many of the resonators from 1 to 67 GHz, using an intermediate frequency bandwidth of 700 Hz and 13 MHz point spacing. From the initial measurement, we select a region of higher coupling devices, corresponding to better matched layer thicknesses. From this region, we select a subset of 16 resonators for 220 GHz characterization.

Proper 220 GHz characterization requires codesign of the resonator microwave structures and measurement standards. We determined the geometric dimensions of the transmission line structures for use with the 50  $\mu\text{m}$  pitch 220 GHz probes. We use Ansys HFSS to roughly match the impedance of the transmission line to 50 ohms. It should be noted that while a 50-ohm design is pursued, a perfect 50-ohm match is not required since all 4 S-parameters will be considered for calibration and measurement. Once we determine the lateral dimensions of the transmission line structure, we create a corresponding calibration kit. For this, the length of the transmission line - from the end of the probe pad to the tapered region - defines a half-thru structure of corresponding length (SFig. 3). This length serves as a standard from which short, open and line structures are defined. To define a multiline transmission line (MTRL) standard, we select line lengths of 0.141, 0.241, 0.441, 0.641, 1.141, 2.341 and 4.741 mm.

We perform calibration to the probe tips by measuring an MTRL calibration kit fabricated on a sapphire wafer. After initial calibration, we perform the second-tier calibration by using the first-tier calibrated system to measure the on-chip calibration kit and the subset of selected devices. Using the second-tier calibration propagation parameters, we translate the device reference plane from the edge of the measurement tick marks placed to the side of the device - used for consistent measurement - to the beginning of the taper region. This accounts for the capacitance, inductance, and resistance associated with the length of the tapered transmission line. It does not, however, remove the probing region where contact of the microwave probes is made. We validate the calibration up to 150 GHz. However, after this threshold the noise becomes too high for use, eliminating the opportunity for examination of the 27th order and adjacent modes.

### 1.3 Effect of layer thickness variation

Changes in relative layer thicknesses yields the observed variability in achieved electromechanical coupling of a specific mode. This is also the cause of the emergence of adjacent modes parallel to the target resonant modes. The electromechanical coupling of the desired thickness shear modes can be approximated by first calculating the ideal electromechanical coupling for the fundamental. To find this, we first account for the properties of the given crystallographic orientation through a (0, -38, 0) degree ZXZ Euler rotation. We use Bond rotation matrices to perform this rotation, corresponding to the desired 128Y cut LN<sup>10</sup>. We assume the applied E field to be in the +X crystal direction, and a pure shear mode corresponding to the  $e_{15}$  electromechanical coupling coefficient. The coupling of the pure fundamental mode is then given by:

$$K^2 = \frac{e_{15}}{\epsilon_r \epsilon_0 c_{55}}$$

Where the effective electromechanical coupling achievable in the resonator is given by:

$$k^2 = \frac{K^2}{1 + K^2}$$

This case is for when the electric field associated with the material strain are in phase with each other. However, for alternating orientations, this is no longer true, as the phase of the E field will swap with the alternating crystal orientations. Thus, we can approximate the relative change in electromechanical coupling as a scaling factor,  $a$ , to the fundamental, where the phase overlap for the acoustic strain and electric field polarization in the stack is given by:

$$a = \frac{\int_0^{x_1} \frac{E(x)T(x)}{E^2(x)T^2(x)} dx + \int_{x_1}^{x_2} \frac{E(x)T(x)}{E^2(x)T^2(x)} dx + \int_{x_2}^{x_3} \frac{E(x)T(x)}{E^2(x)T^2(x)} dx}{\int_0^{\frac{X}{3}} \frac{E(x)T(x)}{E^2(x)T^2(x)} dx + \int_{\frac{X}{3}}^{\frac{2X}{3}} \frac{E(x)T(x)}{E^2(x)T^2(x)} dx + \int_{\frac{2X}{3}}^X \frac{E(x)T(x)}{E^2(x)T^2(x)} dx}$$

where  $x_1$ ,  $x_2$ , and  $x_3$  are the locations of the LN layer interfaces and  $X$  is the total layer thickness.  $E(x)$  is assumed to be either 1 for layers 1 and 3, or -1 for layer 2. The strain is then assumed to be a perfect sinusoidal:

$$T(x) = \sin\left(\frac{n\pi x}{x_1 + x_2 + x_3}\right)$$

where  $n$  is the mode order. Through this, the relative change in electromechanical coupling relative to the ideal, perfectly spaced layers can be examined. By changing the thickness of LN layers 1 and 2 relative to a normalized layer 3 – that is  $0.8x_3 < x_1, x_2 < 1.2x_3$  - the corresponding changes in electromechanical coupling for the 3rd, 9th, 15th and 21st order modes are

calculated. It can be seen that as the 3 relative layer thicknesses become mismatched, the corresponding electromechanical coupling of the mode decreases. For increasing order modes, such as the 21st order, small deviations can result in large shifts. Similar shifts can be seen for adjacent modes, which see increasing coupling with layer variations (SFig. 8 a-b). In the case of the sample selected, we measured frequency variations ranging from 48.8 GHz to 50 GHz for the 9<sup>th</sup> order mode depending on location (SFig. 8 c). This corresponds to thickness variations +/- 10nm or so, which was consistent with the prototype wafer tolerances. While better thickness control would yield more consistent figures of merit (SFig. 8 d), this could be achieved more readily on a production grade process or through localized ion beam trimming. The latter is commonly employed for commercial film bulk acoustic resonators, making it a well established process for industry grade processing.

#### 1.4 Electromagnetic resonance

The measured S-parameter response from the second-tier calibration can be attributed to contributions from electrical contributions from the tapered region leading to the device cavity, mechanical motion induced by piezoelectric electromechanical coupling, and a static electrical capacitance between electrodes in the cavity. These contributions are accounted for in the extraction of the cavity parameters by inclusion in the MBVD model used for the device (SFig. 9). A lumped element model is used for the tapered transmission line from the calibration reference plane to the cavity plane since the length of 35  $\mu\text{m}$  is significantly sub-wavelength for the highest well-calibrated frequency of 150 GHz. For the representation of the mechanical vibrations of the acoustic resonances, 17 series RLC circuit branches are used to represent the prominent acoustic

resonances that appear. Finally, a static capacitance represents the capacitance associated with the interdigitated electrode structure.

To optimize the MBVD model, the circuit model is simulated in Keysight Advanced Design System. Goals for both reflection and transmission parameters, plotted in both magnitude and phase, are established to minimize the root mean square error. First, the electrical response is extracted by setting static capacitance values based on the low frequency response of the device. Then, acoustic branches are added individually from low to high frequencies. Following this, electromagnetic branches and mechanical branches are optimized independently to minimize the root mean square error. The standard deviation of the fit across the frequency range is then used to qualify the model.

From the model, the emergence of the observed electromagnetic resonance can be realized. The primary contributions of this resonance are the series inductance in the tapered line and electrodes and the capacitance of the static branch. In the case where lateral wavelengths of the transducer electrodes are changed, the frequency of the electromagnetic resonance is increased with a decrease in the static capacitance (SFig. 10). In cases where acoustic resonant modes and electromagnetic resonances are co-located, the perceived strength of the acoustic modes can appear higher as energy oscillates between the LC tank and acoustic mode. However, the extracted electromechanical coupling is still determined by the strain charge form.

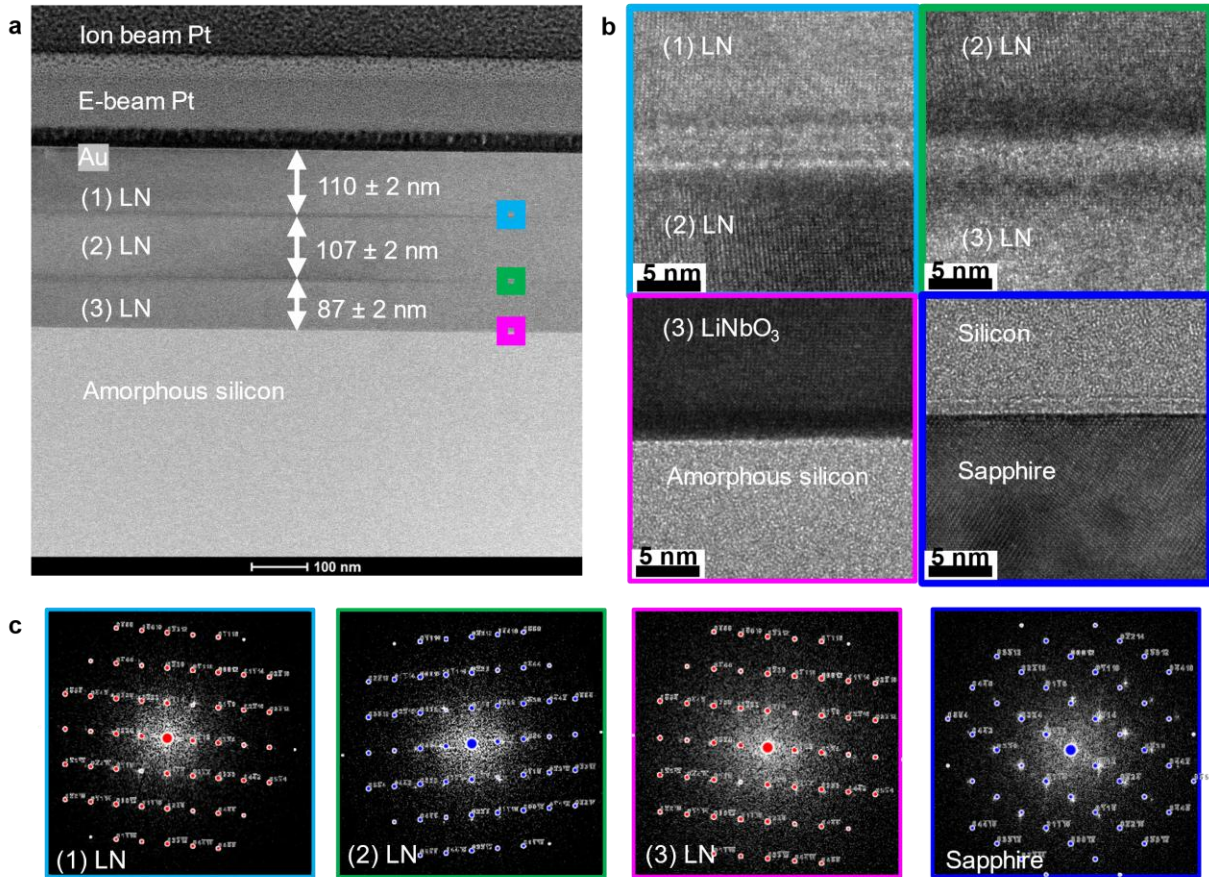
### 1.5 Potential of resonators for filters

To utilize these resonators in compact filters for front end communication systems, we simulate a filter response using the equivalent circuit model of the 49 GHz resonance. We cascade the



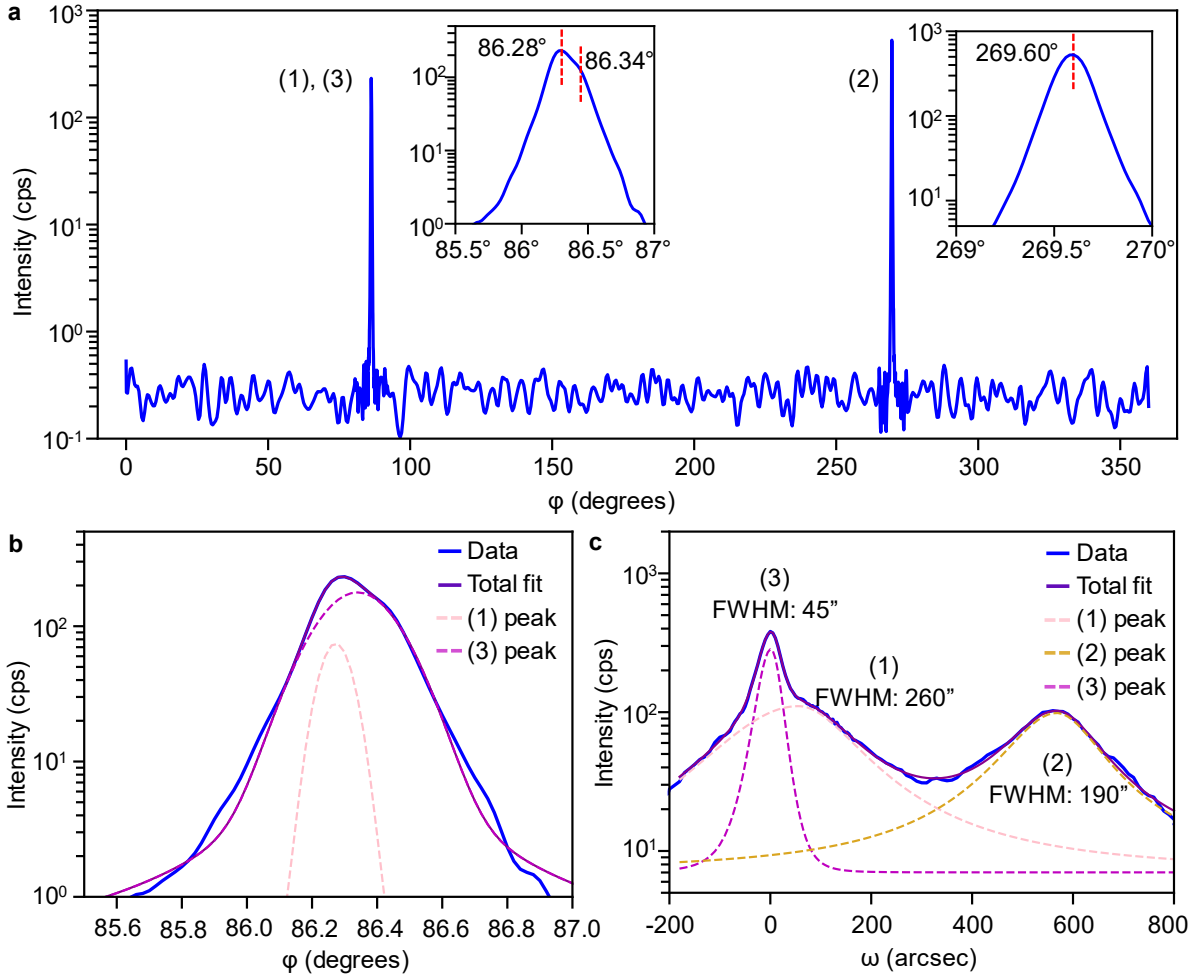
equivalent circuit models in a 3<sup>rd</sup> order ladder configuration (SFig. 12 **a**). In this configuration, a frequency shift is included for series resonators, which can be accomplished via localized thickness trimming using a modified version of the aforementioned ion beam etching process. The simulated response after cascading shunt and series resonators provides 4.6% fractional bandwidth with an insertion loss of 2.4 dB at 50 GHz (SFig. 12**b**). While out of band rejection is moderate, this configuration could be cascaded with electromagnetic stubs to create higher frequency selection and broadband rejection. When we compare this with a commercial cavity filter, the latter certainly offers improved performance. However, this comes at a significantly increased weight of 36 g and form factor of 3900 mm<sup>3</sup> versus ~750 μg and ~0.281 mm<sup>3</sup>. In this case, we select the 49 GHz resonance as a demonstration of this principle since the higher frequency resonances do not have sufficient figures of merit to achieve a useful filter. However, further optimization of the platform with more and thinner layers could conceivably achieve similar results at even higher frequencies.

## Supplementary Figures



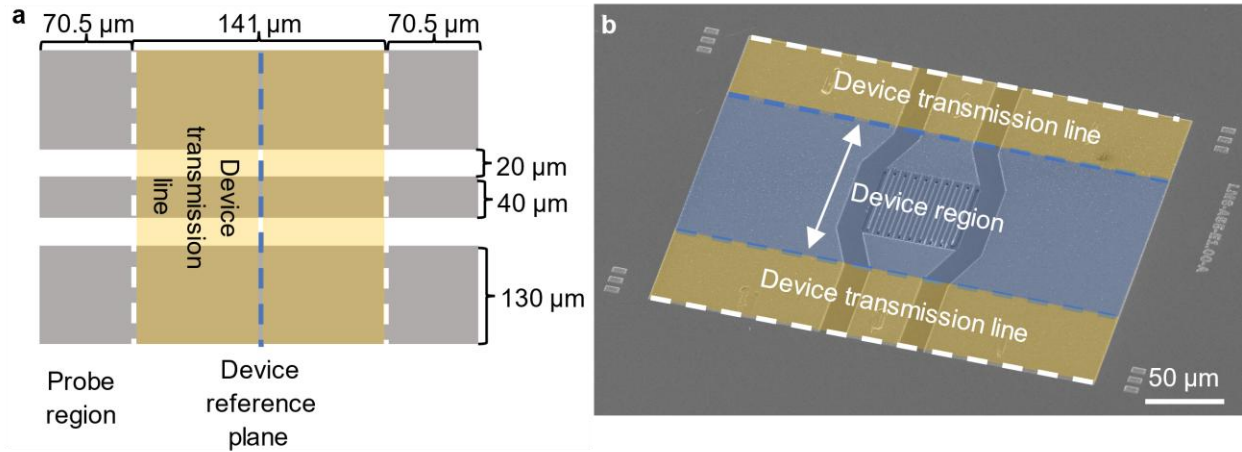
Supplementary Figure 1| **a** Bright field transmission electron microscope micrograph of the multilayer lithium niobate stack, including the amorphous silicon sacrificial layer and added metal layers. The top metal stack of gold and platinum is added to reduce sample charging for imaging purposes. **b** High resolution transmission electron microscope micrographs of all material interfaces. Amorphous bonding residuals can be observed between lithium niobate layers and at the amorphous silicon and sapphire interface. These amorphous layers are located near stress nulls, reducing their impact on the acoustic performance. No amorphous layer is present at the bottom of the lithium niobate layer (3), thanks to the direct deposition of silicon on the lithium niobate layer. **c** Complete electron diffraction patterns for each layer of the stack. Colored dots

correspond to simulated diffraction patterns, which are overlaid with the measured diffraction pattern.

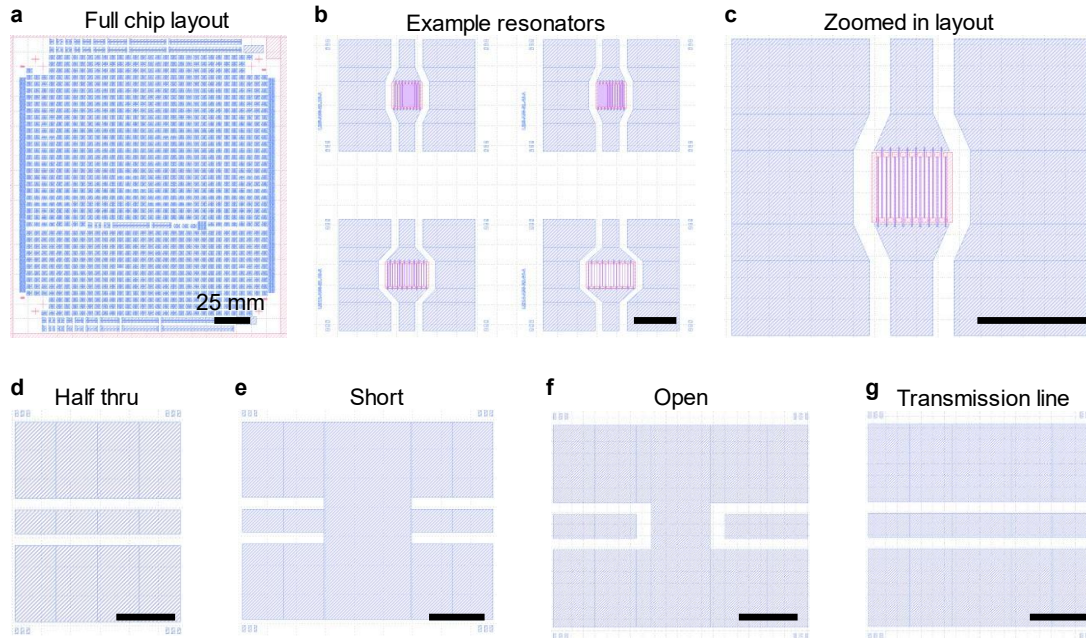


Supplementary Figure 2 | **a**  $\phi$  x-ray diffraction scan of the multilayer stack. Insets show enlarged plots of the two peaks. The left enlarged image shows the existence of two individual peaks, corresponding to layers (1) and (3) of the multilayer stack. **b** Lorentzian fittings of the left  $\phi$  scan peak for the extraction of the in-plane peak locations. **c** Rocking curve x-ray diffraction measurement of the multilayer stack, along with additional Lorentzian fittings for the extraction of full width at half maximum (FWHM) values of the three peaks. The first transferred layer

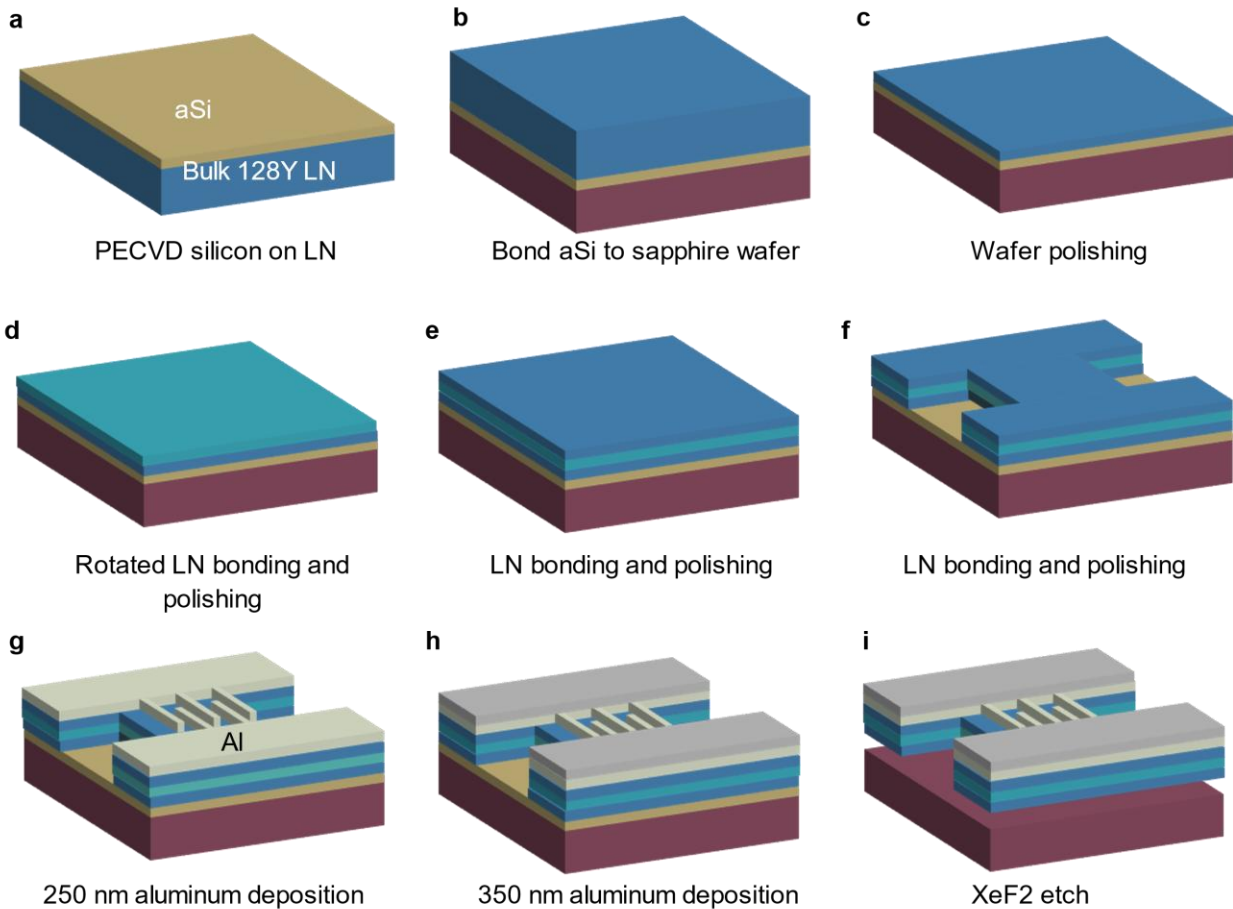
exhibits the lowest FWHM, while later layers exhibit slightly broadened peaks. However, all peaks indicate the maintenance of a single crystal platform for each individual layer.



Supplementary Figure 3 | **a** Illustration of the half-through coplanar waveguide geometry used for the on-chip calibration kit and the device transmission line. The device transmission line region is highlighted in yellow, with a blue dashed line to indicate where the device region reference plane lies. **b** Scanning electron microscope micrograph of a fabricated device. The transmission line structure used in the calibration kit is highlighted in yellow. Additionally, the device region, located between the reference plane, is highlighted in blue.

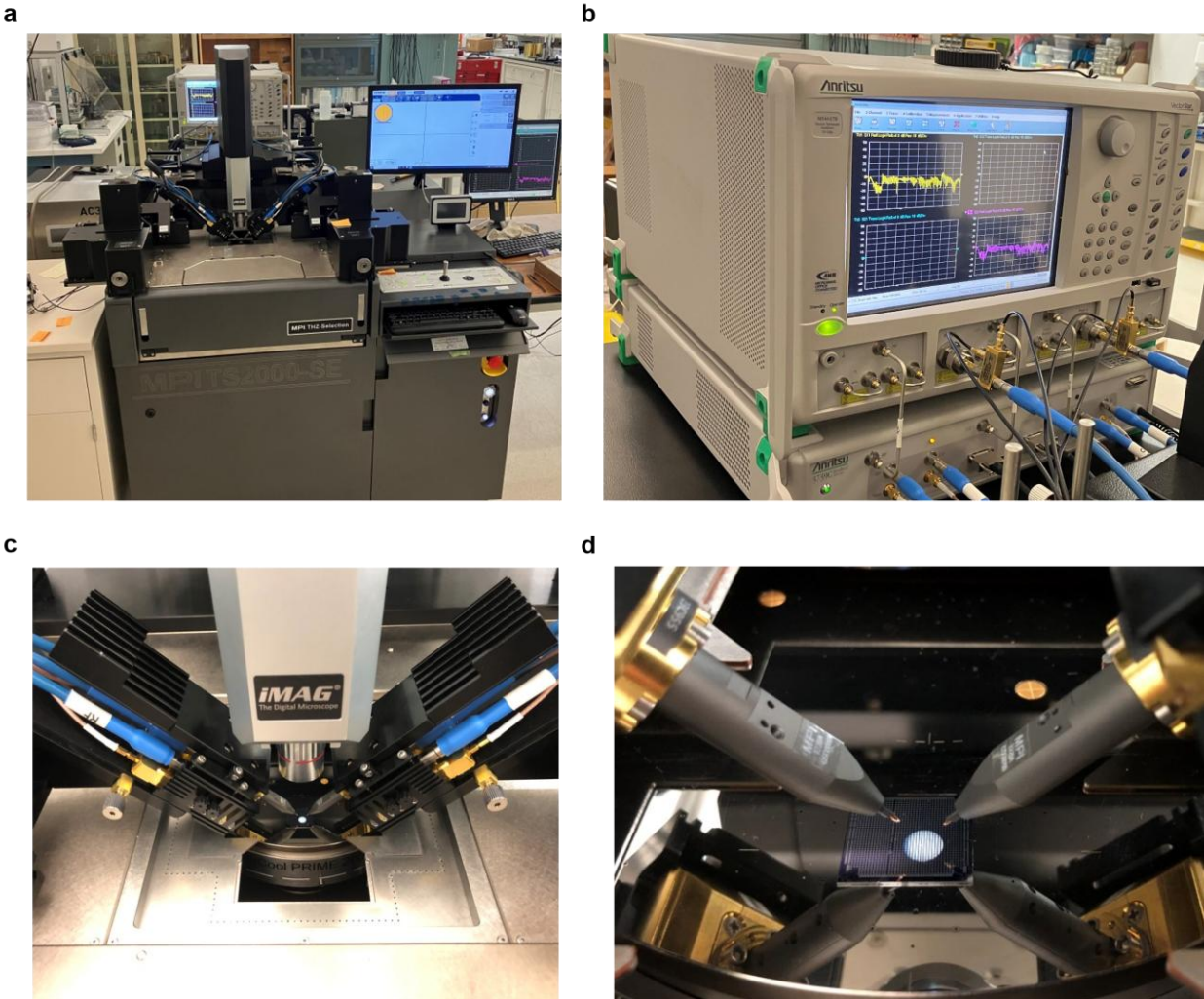


Supplementary Figure 4| **a** Graphic design system (GDS) layout of the array of acoustic resonators. **b** Enlarged example of acoustic resonator layouts, displaying the consistent transmission line structure used and varied geometries of the resonant cavities. **c** Example of the GDS layout of a single resonator. The different colors relate to different lithographic steps or writing settings used. **d-g** Layout of a subset of the on-chip calibration kit. The half-through length is defined by the resonator transmission line. Open and short planes are defined at the center of the half-through length. Transmission line structures are defined by additional length added to the center of the half-through. The scale bar for b-g corresponds to 100  $\mu\text{m}$ .

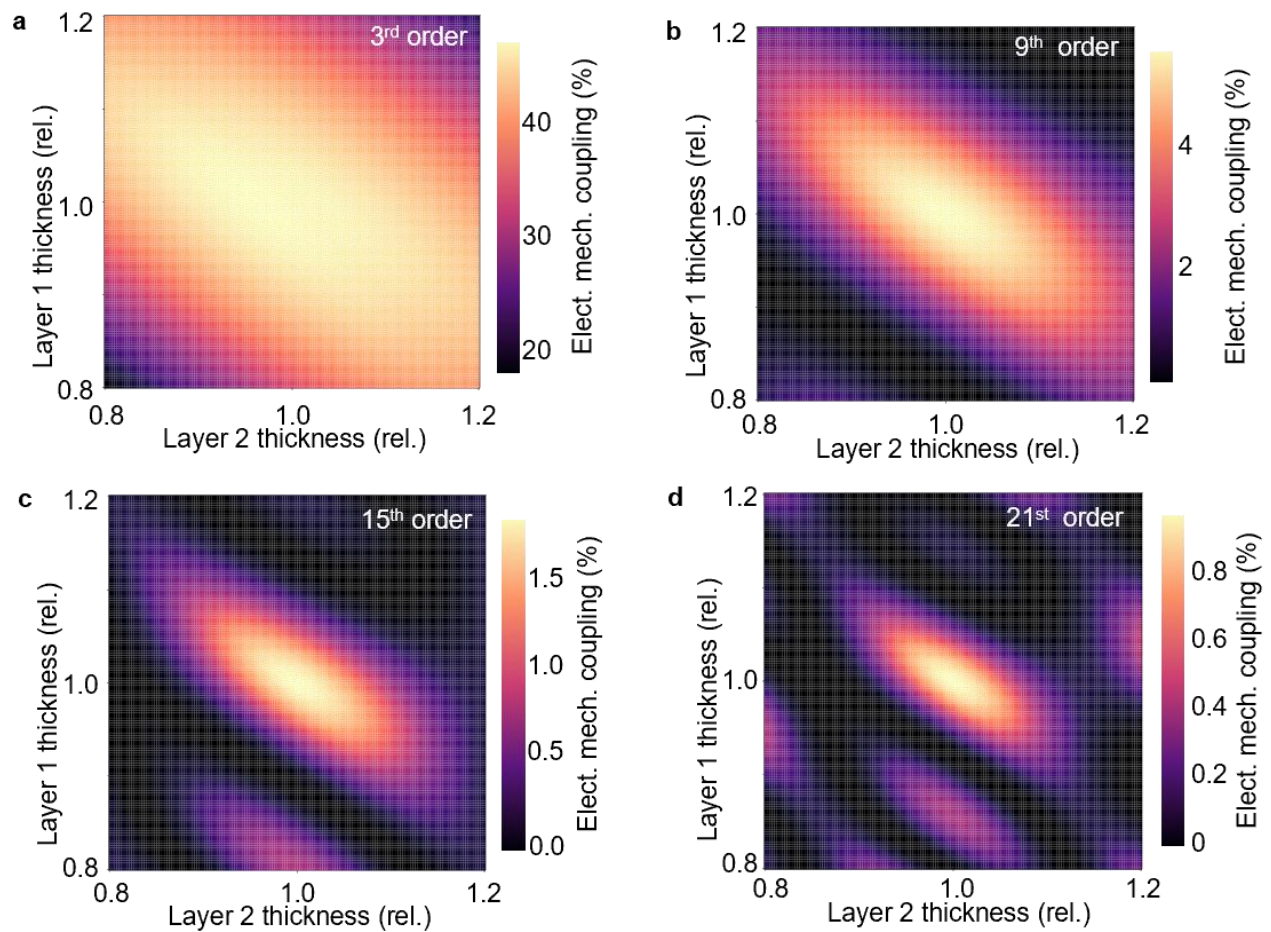


Supplementary Figure 5 | **a-i** Fabrication flow used for device fabrication. a-e summarize the process for achieving the multilayer lithium niobate stack. First, amorphous silicon is deposited on a bulk 128Y cut lithium niobate wafer. This wafer is bonded to the sapphire substrate and then polished with chemical mechanical polishing to the target thickness. The second lithium niobate layer is then transferred to the initial layer and polished, and this is repeated for the third layer. Next, photolithography is used to pattern the sample and used as a mask for argon ion beam etching. After a solvent clean, electron beam lithography is used to pattern the sample. 250 nm of aluminum are evaporated on the sample and lifted off to define the electrode and busline features. Then, a second round of electron beam lithography, aluminum evaporation and lift-off

are used to add 350 nm to the busline regions for probing. Finally, the acoustic cavity is released from the substrate using isotropic xenon difluoride etching.

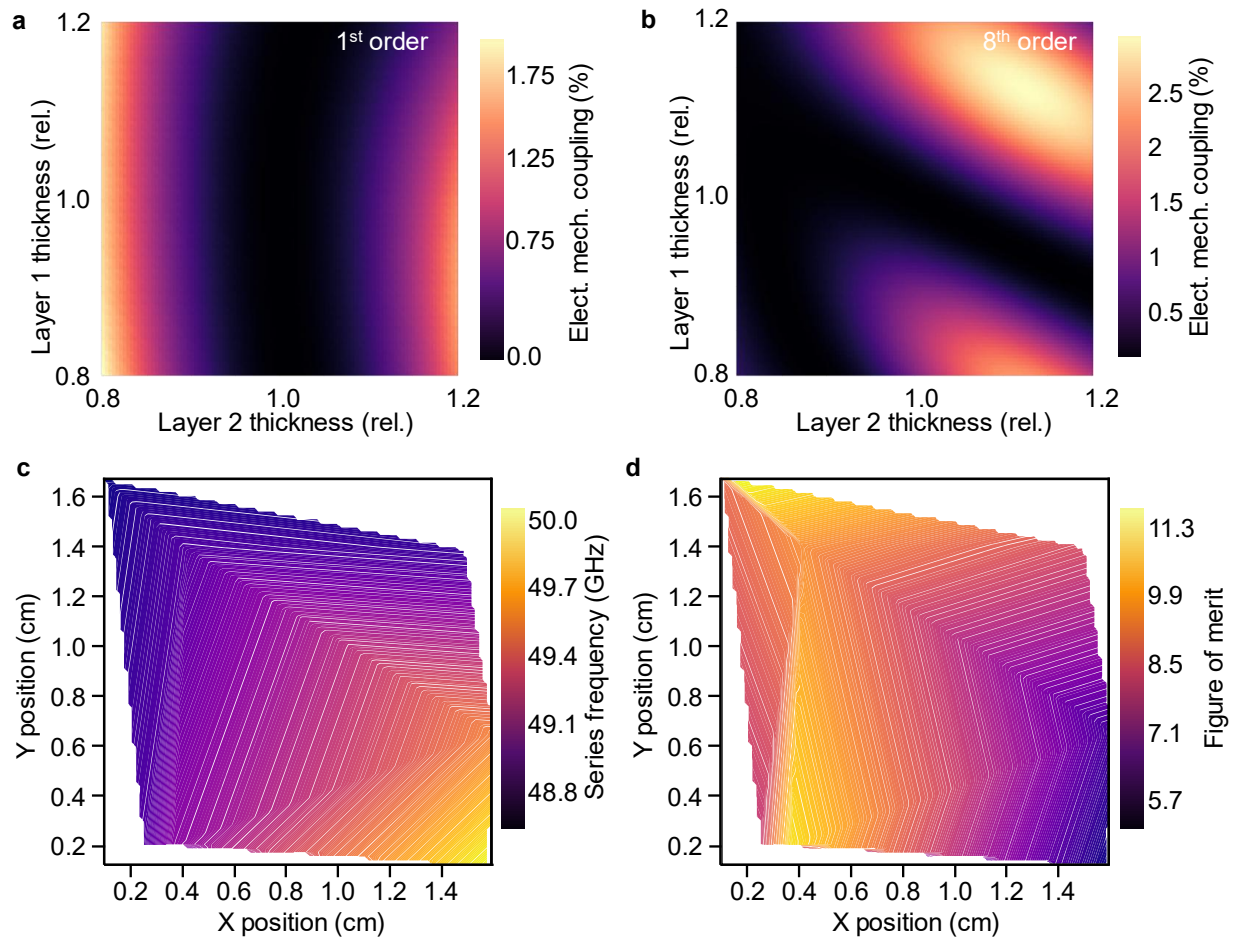


Supplementary Figure 6| Images of the 220 GHz measurement set up. **a**, **b** The probe station (panel **a**) sits in front of the 70 GHz MS4647B vector network analyzer (panel **b**). **c** Extender heads (panel **c**) increase the frequency range to 220 GHz. **d** The extender heads are attached to 50  $\mu\text{m}$  pitch ground signal ground probes (panel **d**) that measure the sample.



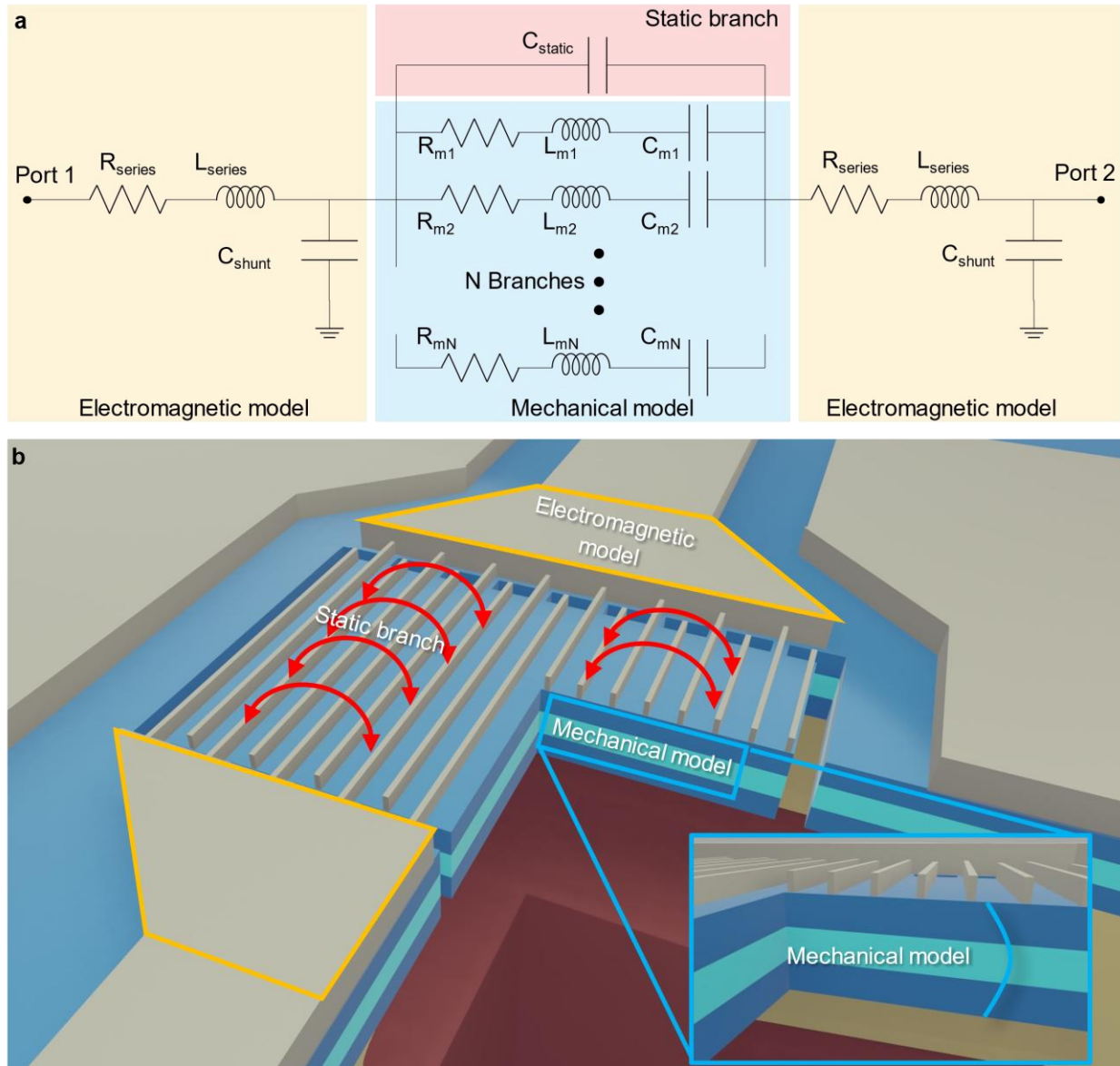
Supplementary Figure 7 | **a-d** Color maps, calculated from first principles of electromechanical coupling as a function of layer thicknesses, relative to a normalized third layer, for the target 3<sup>rd</sup>, 9<sup>th</sup>, 15<sup>th</sup> and 21<sup>st</sup> order modes respectively. Layers 1 and 2 correlate to lithium niobate layers (1) and (2) in transmission electron microscope micrographs. A reduction in coupling can be observed for all modes as the relative thicknesses are moved away from the ideal case of identical individual layer thicknesses. For the highest order modes, additional diminished peaks can be observed for mismatched layers as the phase of the strain and electric field profiles can more easily align for a mismatched case.





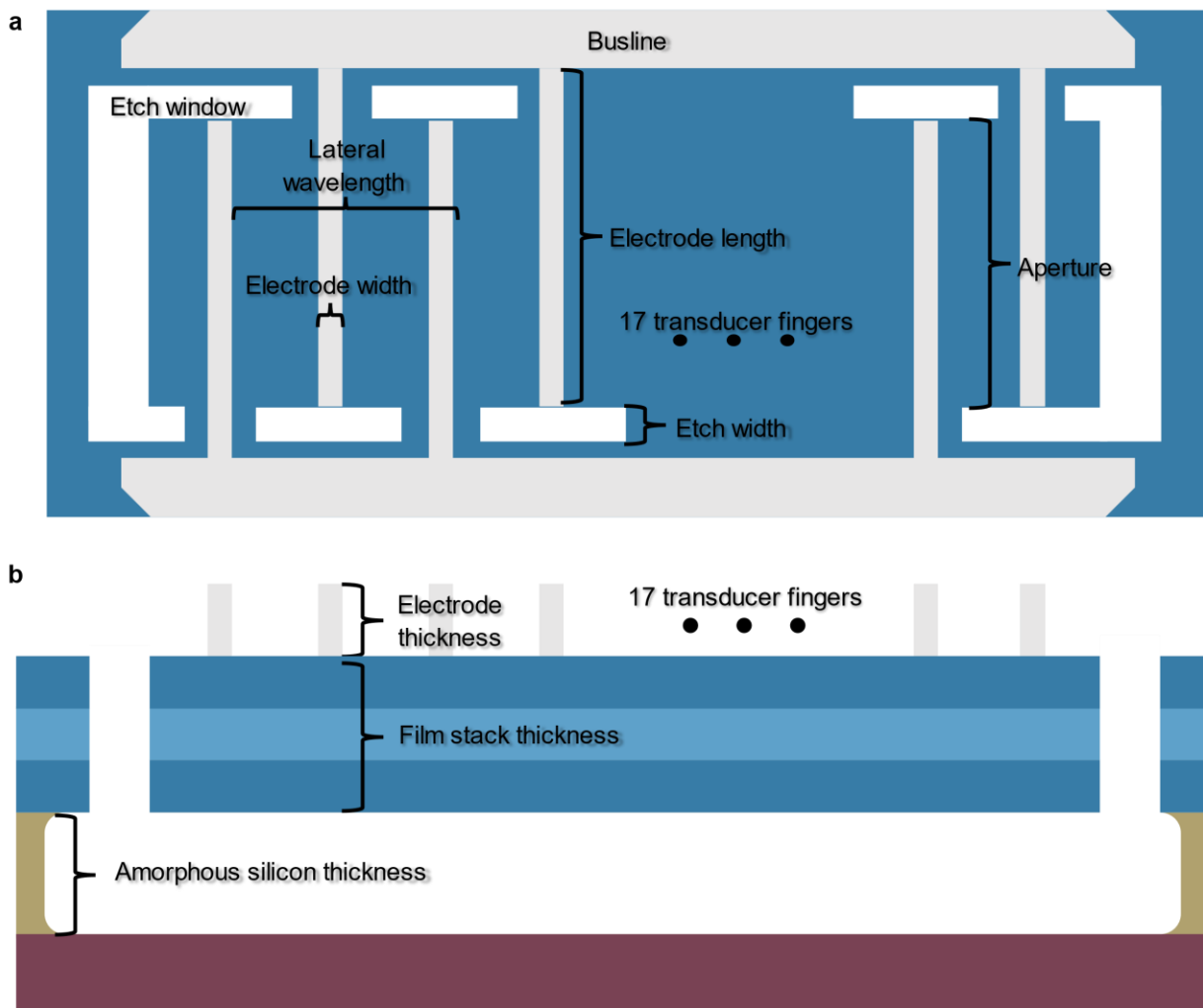
Supplementary Figure 8 | **a-b** Effect of layer thickness mismatch on the 1<sup>st</sup> and 8<sup>th</sup> order thickness shear modes. In the case of the 1<sup>st</sup> order mode, a significant relative shift in the second layer relative to the other layers is required to allow significant coupling into these modes. However, in the case of the 8<sup>th</sup> order, smaller relative shifts allows for a measurable mode to appear. **c** Mapping of series resonant frequency of the 9<sup>th</sup> order mode versus device location on the sample. The shift in series resonance comes largely from the slight variation in total stack thickness, on the order of +/- 10 nm over the sample. **d** Mapping of the perceived figures of merit of the 9<sup>th</sup> order mode for screening devices versus location on the sample. The downward trend towards the bottom right corresponded to a decrease in perceived electromechanical coupling

due to layer mismatch. The perceived values of electromechanical coupling and quality factor used for the screening were extracted directly from the raw data for these tones. This yielded slightly higher values for electromechanical coupling and quality factor than those extracted from fitting, resulting in higher figures of merit.

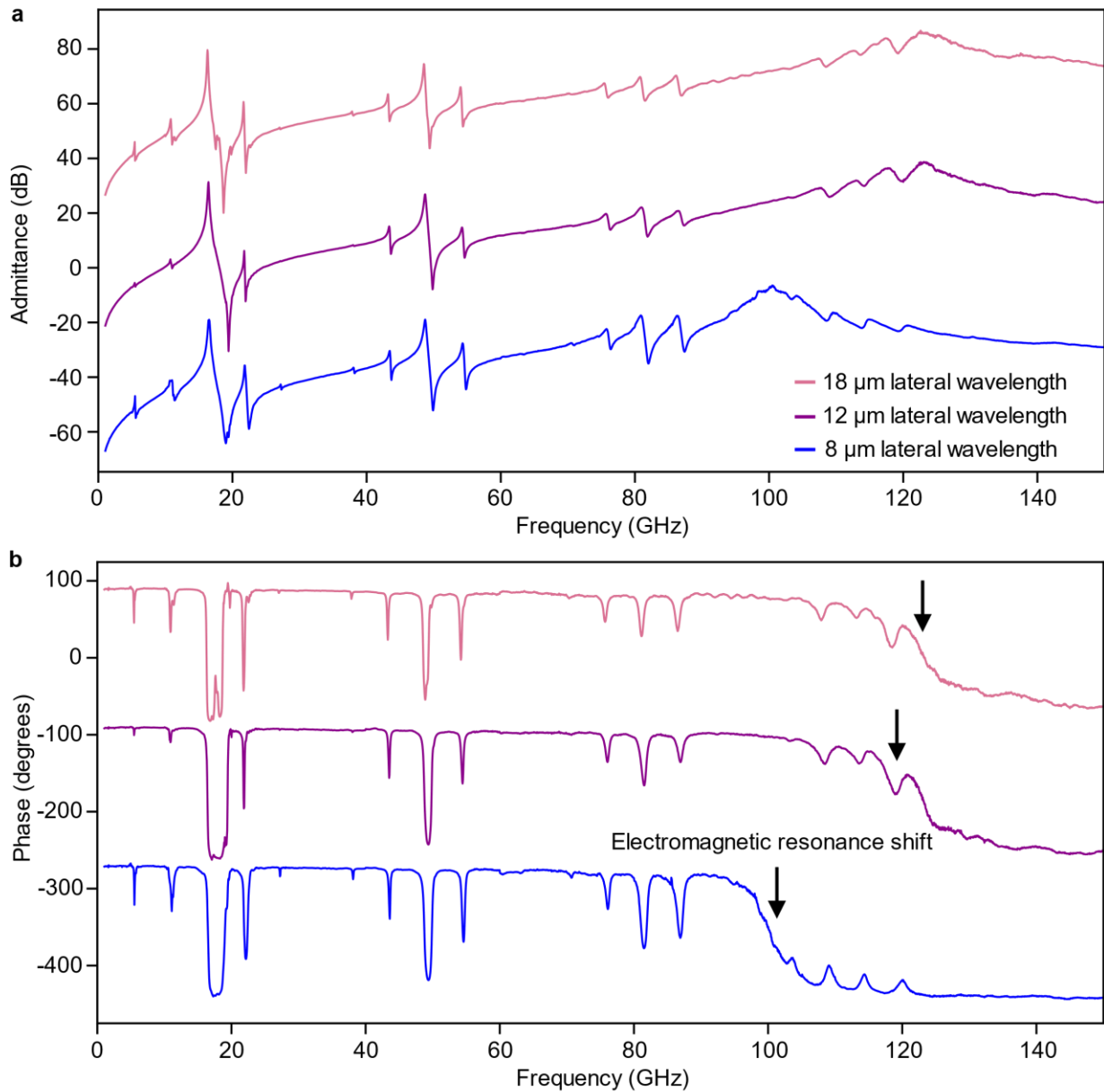


Supplementary Figure 9 | a Modified Butterworth-van Dyke model used for the extraction of acoustic cavity performance parameters. Extracted parameters for the primary resonator are

listed in table 1. **b** Illustration of the components of the model as it relates to acoustic resonant cavity structure. The first and last stages of the model, highlighted in yellow, correspond to the electromagnetic contributions associated with the tapered regions from the calibration plane to the beginning of the acoustic cavity. The static capacitance represents the capacitance associated with electrode feedthrough. The mechanical model consists of  $N=17$  branches to represent the 17 major resonant cavity modes observed in the measurement.



Supplementary Figure 10| **a** Top and **b** side illustrations of important geometrical considerations of resonant cavity design. Parameters for the device used in this work are indicated in table 2.



Supplementary Figure 11| **a,b** Measured admittance and phase for three separate resonators with varied lateral wavelength. Admittance curves are shifted up by 50 dB and phase curves are shifted down by 180 degrees from their nearest neighbor for visualization purposes. The increase

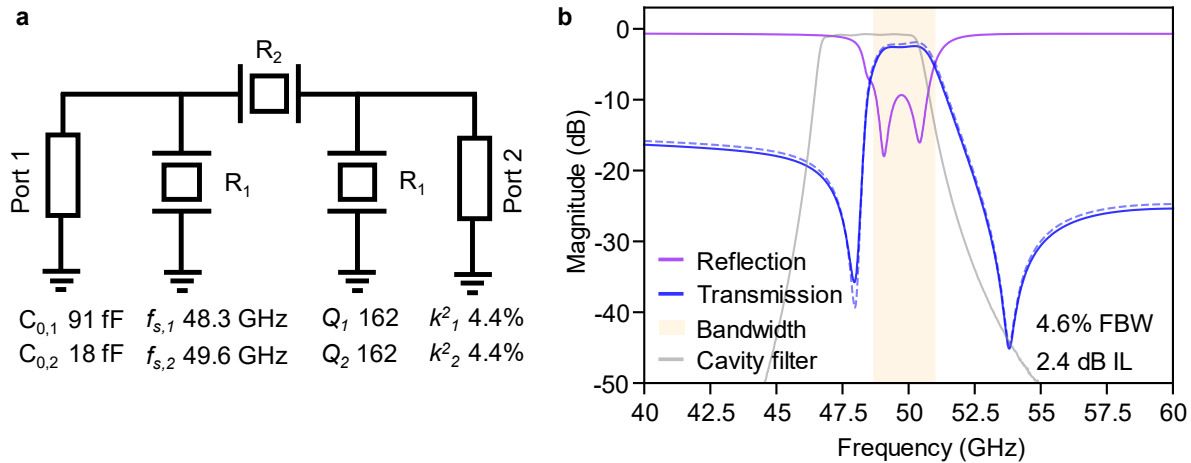
in lateral wavelength results in a decrease in the static capacitance, shifting the electromagnetic resonance to higher frequencies.

Frequency (GHz)	Quality factor	Elect. mech. coupling (%)
5.52	75.3	2.47
11.06	40.0	5.55
16.59	52.2	46.4
21.88	63.3	4.0
27.24	178.5	0.07
38.17	119.9	0.22
43.55	211.6	0.07
49.0	162.1	4.4
54.5	177.0	1.0
70.7	130.4	0.04
76.1	126.8	0.37
81.6	130.7	0.92
87.1	116.7	0.60
103.4	78.0	0.049
108.8	85.7	0.168
114.1	99.7	0.169
119.8	97.8	0.165
Parameter	Value	
$C_0$	45.47 fF	
$R_{series}$	1.139 $\Omega$	
$L_{series}$	28.66 pH	
$C_{shunt}$	9.67 fF	

Table 1| Summary of extracted quality factors and electromechanical coupling values for the 17 strongly coupling acoustic modes.

Parameter	Value/Range
Lateral wavelength	6 - 20 $\mu\text{m}$
Aperture	45, 55, 65 $\mu\text{m}$
Electrode thickness	250, 350 $\mu\text{m}$
Silicon thickness	1 $\mu\text{m}$
Electrode length	50 – 70 $\mu\text{m}$

Table 2| Summary of primary swept cavity parameters for this study.



Supplementary Figure 12 | **a** Configuration of the 3<sup>rd</sup> order ladder filter used to simulate a possible 50 GHz acoustic filter response.  $R_1$  and  $R_2$  denote shunt and series resonators respectively. The measured quality factors and electromechanical coupling are assumed for both series and shunt resonators. The optimized static capacitances and frequencies are included for each resonator type. Parasitic inductance and routing resistance extracted from the MBVD is also included in each resonator model. **b** Simulated response of the ladder filter using the parameters provided in **a**. The achieved 3 dB fractional bandwidth (FBW) is 4.6% and the minimum insertion loss is 2.4 dB. The response of a 47-49 GHz cavity filter from Minicircuits is plotted for comparison. While the cavity filter exhibits improved performance, it comes in at a weight of 36 g and versus approximately 750  $\mu$ g for the simulated filter.